

# Water vapor distribution in protoplanetary disks

Fujun Du and Edwin A. Bergin

*Department of Astronomy, University of Michigan, 500 Church Street, Ann Arbor, MI 48109, USA*  
fdu@umich.edu

## ABSTRACT

Water vapor has been detected in protoplanetary disks. In this work we model the distribution of water vapor in protoplanetary disks with a thermo-chemical code. For a set of parameterized disk models, we calculate the distribution of dust temperature and radiation field of the disk with a Monte Carlo method, and then solve the gas temperature distribution and chemical composition. The radiative transfer includes detailed treatment of scattering by atomic hydrogen and absorption by water of Ly  $\alpha$  photons, since the Ly  $\alpha$  line dominates the UV spectrum of accreting young stars. In a fiducial model, we find that warm water vapor with temperature around 300 K is mainly distributed in a small and well-confined region in the inner disk. The inner boundary of the warm water region is where the shielding of UV field due to dust and water itself become significant. The outer boundary is where the dust temperature drops below the water condensation temperature. A more luminous central star leads to a more extended distribution of warm water vapor, while dust growth and settling tends to reduce the amount of warm water vapor. Based on typical assumptions regarding the elemental oxygen abundance and the water chemistry, the column density of warm water vapor can be as high as  $10^{22} \text{ cm}^{-2}$ . A small amount of hot water vapor with temperature higher than  $\sim 300 \text{ K}$  exists in a more extended region in the upper atmosphere of the disk. Cold water vapor with temperature lower than 100 K is distributed over the entire disk, produced by photodesorption of the water ice.

*Subject headings:* astrochemistry — planetary systems: protoplanetary disks — ultraviolet: planetary systems

## 1. Introduction

Low mass and possibly high mass stars gain additional mass through a circumstellar disk at their late stage of formation. As the disk itself evolves planets are born in the dense dusty mid-plane, hence these systems are called protoplanetary disks. The physical and chemical environments of the disk is thus vital for determining the properties of these planets. Among all the chemical species in a disk, water is one of the most important, because: (1) it may carry most of the oxygen that is available, the only competitors being CO and possibly CO<sub>2</sub> (Favre et al. 2013; Pontoppidan et al. 2014); (2) it may contribute significantly to the heating and cooling of the disk material, hence affecting the dynamics; (3) it may shield the disk material from UV radiation (Bethell &

Bergin 2009); (4) it may aid in the coalescence of dust particles to form planetesimals (Stevenson & Lunine 1988; Ros & Johansen 2013); (5) its relation to the origin and sustaining of life.

Water vapor has been detected in protoplanetary disks through infrared rovibrational and rotational lines (Carr et al. 2004; Carr & Najita 2008; Salyk et al. 2008, 2011; Pontoppidan et al. 2010a,b; Doppmann et al. 2011; Hogerheijde et al. 2011; Riviere-Marichalar et al. 2012; Fedele et al. 2012; Najita et al. 2013). For the most part these observations are spatially and spectrally unresolved, leaving some uncertainty regarding the overall spatial distribution of water vapor within the disk. However, the combination of *Spitzer* and *Herschel* data provide access to transitions arising from a wide range of energy states (ground, 0 K,

to thousands of K); in this case the abundance distribution of water vapor might be inferred using other information to constrain the physical structure (e.g. density and temperature). In one intriguing study, Zhang et al. (2013) infer a warm, narrow, and high column density ring of water at a distance of 4 AU to the central star in TW Hya by fitting to the *Spitzer* and *Herschel* spectra. The water vapor temperatures assumed by these observers for fitting their data apparently show a dichotomy. The cold water vapor has temperatures  $\lesssim 100$  K, and the hot/warm water vapor has temperatures of 200–1500 K. Though never directly spatially resolved, model fittings in these works suggest that the hot water are concentrated in a small region close to the central star, and the cold water are distributed over an extended region in the outer disk.

A few questions naturally arise. (1) How are the water molecules formed in these disks? (2) What is the interstellar heritage of water in the disk? Did all water form in the prestellar core prior to stellar birth? (3) What environmental factors determine the presence of water, and which region and which evolution stage of the disk does the observed water trace? (4) Where do these water molecules ultimately go? (5) Are they related to the water found on planets and comets, and if related, how? The present work will not be able to answer all these questions, but will only contribute to the understanding of questions 1 and 3. Some recent studies related to question 2 and 5 can be found in Furuya et al. (2013), Cleeves et al. (2014), and Albertsson et al. (2014); see also the review by van Dishoeck et al. (2014).

Among the many modeling efforts devoted to the chemistry of protoplanetary disks (for recent reviews, see Henning & Semenov 2013 and Dutrey et al. 2014), a few have focused on gaseous water. In Glassgold et al. (2009) high water abundances is obtained in the molecular transition layer of the inner disk heated by X-rays. They emphasize the role of  $\text{H}_2$  formation, since  $\text{H}_2$  is a precursor of water. Bethell & Bergin (2009) point out that when dust is settled, water becomes the dominant absorber of UV photons, shielding itself from UV dissociation. This self-shielding effect also limits the column density of warm water vapor to  $\sim 10^{18} \text{ cm}^{-2}$  and that of OH to  $\sim 2 \times 10^{17} \text{ cm}^{-2}$ . The model of Woitke et al. (2009b) shows that

in Herbig Ae protoplanetary disks water is distributed in three regions with distinct properties: a deep warm region, an irradiated hot region, and a photodesorbed cold region. Kamp et al. (2013) caution that the interpretation of the observed water emission is affected by uncertainties in the chemical input data and radiative transfer. The recent work of Ádámkovics et al. (2014) focus on the role played by the photodissociation of water and OH. In their model warm water is limited to the inner 4 AU of the disk.

In this work we follow a parameterization approach to study the chemistry of warm water vapor. Our goal is to identify the main stellar and disk parameters that determine the water repository, specifically we clarify the role of water self-shielding in maintaining its abundance, and in this paper we are *not* aiming to reproduce any specific observational results, which will be the content of a follow-up work. Section 2 contains description of a new code we have created from scratch for this study. In section 3 we present the results, and we conclude our paper in section 4.

## 2. Details of the Modeling

### 2.1. Code Description

The layout of our code<sup>1</sup> is similar to the PRODIMO code (Woitke et al. 2009a). Given a distribution of gas and dust, we first solve the dust temperature distribution with a Monte Carlo method based on the strategy of Bjorkman & Wood (2001) (see also Baes et al. 2005; Bruderer et al. 2012), in which the dust temperature of a spatial cell is updated each time a photon packet cross this cell; this strategy is also adopted in the RADMC code (Dullemond & Dominik 2004a). Although the geometry in our code is symmetric with respect to rotation around the central axis and reflection about the midplane, the photon propagation is done in full three dimensions. We have not yet implemented the diffusion approximation (Min et al. 2009) for the highly shadowed region where the photon statistics is low, and we mitigate this by allowing a large number ( $\sim 10^7$ ) of photon packets in the Monte Carlo. The whole spectrum (from UV to sub-millimeter) of the cen-

<sup>1</sup>Our code is publicly available at <https://github.com/fjdu/rac-2d>

tral star is used as input. Observation and modeling of  $\text{H}_2$  fluorescence have shown that Ly  $\alpha$  emission can dominate the UV spectrum (Bergin et al. 2003; Herczeg et al. 2004; Schindhelm et al. 2012). In this case, the resonant scattering by atomic hydrogen in the photodissociated regions is also important, and we treated this similar to Bethell & Bergin (2011b). To increase the signal-to-noise ratio of line features like Ly  $\alpha$ , a smaller energy is used for photon packets when its frequency falls into the line profile. We also include the absorption of UV photons by water. Since the abundance of atomic hydrogen and water is affected by chemistry, the whole process has to be iterated, which is slow but affordable. A byproduct of the radiative transfer is the distribution of radiation field over the whole disk, which will be used as input for chemistry and gas thermal balance.

After establishing the dust temperature distribution, we evolve the disk chemistry for 1 Myr. Since the heating and cooling processes are coupled with chemistry, the gas temperature is evolved in tandem with chemistry based on the heating and cooling rates. Namely, we solve the following set of ordinary differential equations (ODEs)

$$\begin{aligned} \frac{d}{dt}X_i &= P_i(X;T) - D_i(X;T), \quad i = 1, \dots, N, \\ \frac{d}{dt}T &= (\Gamma - \Lambda)/C_v, \end{aligned} \quad (1)$$

where  $X_i$  is the abundance of species  $i$ ,  $P_i$  and  $D_i$  are the production and destruction rates of this species, which are functions of the chemical abundances and temperature (and other physical parameters), and  $N$  is the total number of species.  $C_v = 3k_B/2$  is the volume-specific heat capacity of an ideal gas, where  $k_B$  is the Boltzmann constant. The exact value of  $C_v$  is not important, because we are only concerned with the equilibrium temperature, rather than the rate of temperature change. The heating and cooling rates are contained in  $\Gamma$  and  $\Lambda$ . We do not need a separate set of equations to account for the elemental conservation, since elements are automatically conserved within numerical tolerance. For solving the above set of ODEs, we use the DLSODES solver of the ODEPACK<sup>2</sup> package (Hindmarsh 1983), which makes

use of the sparse structure of the chemical network.

The initial chemical composition is listed in Table 1. The gas temperature is set to the dust temperature at  $t = 0$ , and usually reaches steady state within a short period. We note that the chemistry cannot always reach a steady state within 1 Myr, and may still evolve at time scale  $\gtrsim 10^8$  yr.

We could also solve the chemical equilibrium (or rather quasi-equilibrium) and thermal equilibrium independently. But in such an approach iteration for each single grid point will be needed to achieve a joint convergence, which may pose some numerical issues and takes more CPU time, while in our approach thermal equilibrium is guaranteed as far as the heating/cooling time scale is shorter than the time scale of interest ( $\sim 1$  Myr).

One note about the global iteration in our code. For the radiative transfer in the first iteration, only dust is assumed to be present. This gives a distribution of dust temperature and radiation intensity over the whole disk. Based on this the chemistry and gas temperature is solved on the grid points in a downward (i.e. from surface to midplane) then outward (from close to the central star to the disk outer edge) order. This order has the advantage that the self-shielding of  $\text{H}_2$  and CO can be updated each time a grid point has been calculated during one iteration. The radiative transfer is redone before each chemical and thermal calculation of the whole disk, to take into account the effects (H scattering, water absorption) due to updated chemical composition. The changes in the radial water abundance profile at different vertical height as the iteration proceeds will be described later in Section 3.6. Since the code has a Monte Carlo component (for the radiative transfer) built in, perfect convergence is not expected.

## 2.2. Chemical Network

We use the full UMIST RATE06 network (Woodall et al. 2007) for our gas phase chemistry. Details for the implementation of this network can be seen in that paper. In addition, we include dissociation of  $\text{H}_2\text{O}$  and OH by Ly  $\alpha$  photons, adsorption of major gas phase species onto the dust grain, and desorption of species on the dust grain surface either thermally, or induced by cosmic-rays and UV photons. Two-body reactions

<sup>2</sup><http://www.netlib.org/odepack/>

on the dust grain surface are also included, leading to the formation of  $\text{H}_2\text{O}$ ,  $\text{CH}_3\text{OH}$ ,  $\text{CH}_4$ , etc. The surface network is taken from Hasegawa et al. (1992). Recombination of ions with charged dust grains is included. In total the chemical network has 467 species and 4801 reactions. We describe some reaction types of special importance in the following.

### 2.2.1. Adsorption

The adsorption rate of species X is

$$R_{\text{ad}}(\text{X}) = s\sigma v_{\text{T}} n_{\text{dust}}, \quad (2)$$

where  $s$  is the sticking coefficient,  $\sigma$  is the cross section of dust particles,  $v_{\text{T}}$  is the thermal speed of species X, and  $n_{\text{dust}}$  is the density of dust particles. We have

$$\sigma = \pi a^2, \quad v_{\text{T}} = \sqrt{\frac{8k_{\text{B}}T_{\text{gas}}}{\pi m_{\text{X}}}}, \quad (3)$$

where  $a$  is the average radius of dust particles,  $k_{\text{B}}$  is the Boltzmann constant, and  $m_{\text{X}}$  is the mass of a particle of X.

We calculate the sticking coefficient using a formula from Chaabouni et al. (2012)

$$s = \frac{1 + T_{\text{gas}}/(15\tilde{m}_{\text{X}})}{[1 + T_{\text{gas}}/(38.5\tilde{m}_{\text{X}})]^{2.5}}, \quad (4)$$

where  $\tilde{m}_{\text{X}}$  is the mass number of X. The numbers in the above formula are interpolated from the parameters for nonporous amorphous solid water ice and silicate dust in Chaabouni et al. (2012). The effect of using this formula rather than the commonly used constant value of one is most important for atomic H at high temperatures. If a constant value is used, the formation of  $\text{H}_2$  may heat the gas to unrealistically high temperatures in the photodissociated region.

### 2.2.2. Thermal Desorption

The thermal desorption rate is

$$k_{\text{evap,th}} = \nu e^{-E_{\text{des}}/T_{\text{dust}}}, \quad (5)$$

where  $\nu$  is the characteristic vibrational frequency of species X on the dust grain surface (Hasegawa et al. 1992),

$$\nu = \sqrt{\frac{2n_{\text{S}}E_{\text{des}}}{\pi^2 m_{\text{X}}}},$$

$n_{\text{S}}$  being the number density of surface sites, usually taken to be  $10^{15} \text{ cm}^{-2}$ , and  $E_{\text{des}}$  is the desorption energy of species X, for which we adopt the values from Garrod et al. (2008). Typically  $\nu$  is of the order of  $10^{12} \text{ Hz}$ .

### 2.2.3. Photodesorption

The yield of a species on the dust grain surface per incident UV photon can be empirically written as (Öberg et al. 2009a,b)

$$Y = (a + b \times T_{\text{dust}})(1 - e^{-x/l}), \quad (6)$$

where  $x$  is the thickness of the ice, and  $a$ ,  $b$ , and  $l$  may be approximated as constants, which are determined experimentally. The UV flux is calculated in the radiative transfer part of the code.

For  $\text{H}_2\text{O}$ ,  $\text{CO}$ , and  $\text{CO}_2$ , we use the measured value of the  $(a, b, l)$  parameters from Öberg et al. (2009a,b):

$$\text{H}_2\text{O} : 1.3 \times 10^{-3}, 3.2 \times 10^{-5}, 2,$$

$$\text{CO} : 2.7 \times 10^{-3}, 0, 1,$$

$$\text{CO}_2 : 2 \times 10^{-3}, 0, 3.$$

For all the other species, we assume  $a = 10^{-4}$ ,  $b = 0$ , and  $l = 1$ .

### 2.2.4. Cosmic-ray Desorption

Cosmic-ray desorption is important for the deep and cold region of the disk. We adopt the treatment of Hasegawa & Herbst (1993), in which a dust grain is assumed to be episodically heated by cosmic-rays to a high temperature (70 K) followed by evaporation of a large fraction of its ice mantle. Namely

$$k_{\text{evap,CR}} = k_{\text{evap,th}}(T=70 \text{ K}) f(70 \text{ K}), \quad (7)$$

where  $f(70 \text{ K})$  is the fraction of time for the dust to spend at temperature  $\sim 70 \text{ K}$ , which is estimated to be  $3.16 \times 10^{-19}$  for a dust grain size of  $0.1 \mu\text{m}$  and a total cosmic-ray ionization rate of  $\sim 10^{-17} \text{ s}^{-1}$  (Leger et al. 1985). The cosmic-ray intensity is attenuated with an  $e$ -fold column density of  $96 \text{ g cm}^{-2}$  (Umebayashi & Nakano 1981), and the induced evaporation rate is scaled down accordingly. A different grain size distribution and cosmic-ray spectrum would produce different values for these parameters, though many details are subject to large uncertainties (Cleeves et al. 2013).

### 2.2.5. $H_2$ Formation

Since H participates in many surface reactions other than the formation of  $H_2$ , we cannot simply assume that all the H atoms adsorbed onto the dust grain are converted into  $H_2$  molecule. So we treat the formation of  $H_2$  on dust grain surface as a normal two-body reaction between two H atoms. Hence the formation rate (i.e. the number of  $H_2$  molecules formed per unit volume per unit time) is

$$R(H_2) = k_{HH} n^2(H_{gr}), \quad (8)$$

where  $n(H_{gr})$  is the number density of H atoms on the grain surface, which recombine with a rate coefficient

$$k_{HH} = \frac{\nu_H}{n_{dust} N_S} e^{-E_{diff}/T_{dust}}, \quad (9)$$

in which  $E_{diff}$  is the energy barrier for migrating over the dust grain surface, usually taken to be half of the desorption energy,  $N_S$  is the number of sites per dust grain, and  $n_{dust}$  is the number density of dust particles. At low temperatures, quantum tunneling becomes important, and the exponential part will be replaced by (Hasegawa et al. 1992)

$$e^{-2a_{diff}\sqrt{2m_{\chi}E_{diff}}/\hbar},$$

where  $a_{diff}$  of the order of 1 Å is the barrier width for surface migration. We assume H atoms on dust grain surface are chemisorbed, and set the desorption energy to  $10^4$  K according to Cazaux & Tielens (2004). Physisorption alone is not enough to account for the abundance of  $H_2$  in the hot regions of the interstellar medium (ISM; Cazaux et al. 2005). Note that if we assume all the adsorbed H atoms are converted into  $H_2$ , then  $R(H_2)$  simply becomes half of the adsorption rate of H as calculated from equation (2).

### 2.2.6. Photodissociation of $H_2O$ and OH

The photodissociation of  $H_2O$  and OH by generic ISM UV field are included in the UMIST RATE06 network. In addition, we include the dissociation by Ly  $\alpha$  photons using the cross sections from van Dishoeck et al. (2006), with  $\sigma_{H_2O} = 1.2 \times 10^{-17} \text{ cm}^2$ , and  $\sigma_{OH} = 1.8 \times 10^{-18} \text{ cm}^2$ . The local UV (including Ly  $\alpha$ ) flux in the disk is determined from the radiative transfer. The shielding effect of  $H_2O$  is included in the radiative transfer.

### 2.2.7. Photodissociation of CO and $H_2$

The photodissociation of CO is included in the UMIST RATE06 network. For  $H_2$ , we use a rate coefficient of  $4 \times 10^{-11}$ . The self-shielding of CO and  $H_2$  are considered based on the formulation of Visser et al. (2009) and Draine & Bertoldi (1996), respectively.

### 2.2.8. Photodissociation of Other Species

For other species in the UMIST network, their photodissociation rates are calculated based on the formula given in Woodall et al. (2007)

$$G_0 \alpha \exp(-\gamma A_V), \quad (10)$$

where  $G_0$  is the unattenuated UV continuum intensity at each location of the disk relative to the standard ISM value. Namely,  $G_0$  is calculated from the stellar spectrum assuming only inverse-square-law dilution. The attenuation due to dust and possibly water is included in the  $A_V$  parameter, which is calculated by comparing the local actual UV field (obtained from Monte Carlo radiative transfer) with the unattenuated one

$$A_V = \max(0, -1.086 \ln [F_{UV,att}/F_{UV,unatt}]). \quad (11)$$

Such a treatment is similar to Fogel et al. (2011).

## 2.3. Heating and Cooling Processes

### 2.3.1. Photoelectric Heating

For the heating rate due to small grains and polycyclic aromatic hydrocarbons (PAHs) we use the formula from Bakes & Tielens (1994)

$$\Gamma_{pe} = 10^{-24} \epsilon G_0 n_H, \quad (12)$$

with unit  $\text{erg s}^{-1} \text{ cm}^{-3}$ .  $\epsilon$  is given by

$$\epsilon = \frac{4.87 \times 10^{-2}}{1 + 4 \times 10^{-3} (G_0 T^{1/2}/n_e)^{0.73}} + \frac{3.65 \times 10^{-2} (T/10^4)^{0.7}}{1 + 2 \times 10^{-4} (G_0 T^{1/2}/n_e)}. \quad (13)$$

The PAH abundance used by Bakes & Tielens (1994) is  $1.6 \times 10^{-7}$  relative to H. We take into account the effect of dust settling and growth on this heating rate by scaling down the above rate with a factor equal to the dust-to-gas mass ratio relative to the ISM value (0.01), though the actual amount of PAH in disks is uncertain.

### 2.3.2. Chemical Heating and Cooling

Chemical reactions can release or absorb energy. The heating/cooling due to chemical reactions can be important for keeping the model self-consistent, and has been considered in some of the previous works (see, e.g., Glassgold & Langer 1973; Dalgarno & Oppenheimer 1974; Hollenbach & McKee 1979; Glassgold et al. 2012). We include the contribution to energy balance from reactions involving the major abundant species. The exothermicity or endothermicity of these reactions are calculated based on the enthalpy of the formation of the reactants and products using the following formula

$$\Delta H = \sum \nu_i \Delta_f H^o(i), \quad (14)$$

where the sum is over the reactants and products in a reaction,  $\nu_i$  is the stoichiometric coefficient (negative for reactants and positive for products), and  $\Delta_f H^o(i)$  is the enthalpy of formation of a species.  $\Delta H > 0$  means the reaction is endothermic. The contribution of a reaction to the heating/cooling rate is  $k\Delta H$ , where  $k$  is the reaction rate. The enthalpy of formation of chemical species are slowly changing functions of temperature and pressure. For our purpose it suffices to use the values measured at standard condition (i.e.  $p = 1$  bar,  $T = 298$  K). The thermochemical data are taken from the NIST webbook<sup>3</sup>, Binnewies & Milke (2002), Vandooren et al. (1991), and Nagy et al. (2010). In total 591 reactions are included to contribute to the gas heating/cooling.

### 2.3.3. Heating by $H_2$ Formation

Similar to Sternberg & Dalgarno (1989) and Röllig et al. (2006), we assume one third of the energy released ( $= 4.5$  eV) in the formation of a  $H_2$  molecule from combination of two H atoms are converted into heat of the gas. The corresponding heating rate is

$$\Gamma_{H_2 \text{ form}} = 2.4 \times 10^{-12} \text{ erg } R(H_2), \quad (15)$$

where  $R(H_2)$  (see equation (8)) is the formation rate of  $H_2$  in unit of  $\text{cm}^{-3} \text{ s}^{-1}$ .

<sup>3</sup><http://webbook.nist.gov/chemistry/>

### 2.3.4. Heating by Viscous Dissipation

We use the usual  $\alpha$ -prescription. The heating rate is

$$\Gamma_{\text{vis}} = \frac{9}{4} \alpha \rho c_s^2 \omega_K, \quad (16)$$

where  $\rho$  is the mass density of the gas,  $c_s$  is the sound speed, and  $\omega_K$  is the Keplerian angular velocity.

Usually  $\alpha$  is assumed to be a constant of the order of  $0.01 - 1$ . As noted by Woitke et al. (2009a), the heating rate calculated from equation (16) can become unphysical and gives very high temperature ( $> 10^4$  K) when the density is very low. Hence the calculated high temperature in the top layers of the disk may not be trusted, though this does not affect our goal of study, which is focused on the deeper shielded region. Thus we use the analytical formula of Bai & Stone (2011) fitted from non-ideal magnetohydrodynamical simulations

$$\alpha = \frac{1/2}{[(2500/Am^{2.4} + (8/Am^{0.3} + 1)^2)^{1/2}]}, \quad (17)$$

$$Am = n_{\text{ion}} \beta_{\text{ion}} / \Omega,$$

where  $n_{\text{ion}}$  is the ion density,  $\beta_{\text{ion}}$  is the ion-neutral collision rate, and  $\Omega$  is the local Kepler angular velocity. At the surface of the disk where the density is low, the ambipolar diffusion parameter  $Am$  will be small and so will  $\alpha$  ( $\sim 10^{-4}$ ), which will partially alleviate the problem of temperature getting unphysically high.

### 2.3.5. Heating by Cosmic-ray and X-ray

The cosmic-ray heating rate is (Bruderer et al. 2009a)

$$\Gamma_{\text{CR}} = 1.5 \times 10^{-11} \times \zeta_{\text{CR}} n_{\text{gas}}, \quad (18)$$

where  $\zeta_{\text{CR}}$  is the cosmic-ray flux, and  $n_{\text{gas}}$  is the gas density.

For the X-ray heating, we calculate the X-ray photoelectric cross sections for the gas and dust using the interpolation table in Bethell & Bergin (2011a) assuming a representative X-ray photon energy of 1 keV (corresponding to a  $10^7$  K black body), and assume that each ion pair release 18 eV into the gas (Glassgold et al. 2012). The total X-ray flux from the central star is taken to be  $10^{-3} L_{\odot}$ . The X-ray intensity at each location is attenuated by the column towards the central

star, similar to Glassgold et al. (2004) (see also Glassgold et al. 1997). The contribution of X-ray to the ionization rates are treated similar to Bruderer et al. (2009b), namely, we enhance the cosmic-ray ionization rates by the calculated X-ray ionization rates. As remarked by Bethell & Bergin (2011a), the scattered diffusion of X-ray with energy  $\sim 1 - 2$  keV is not important, though a scattered hard X-ray field can be important even deep in the midplane, especially when the cosmic-ray intensity has been suppressed by the stellar wind of the central star (Cleeves et al. 2013). Hence our simple treatment tends to underestimate the X-ray ionization rate. Aresu et al. (2011) find that a high X-ray luminosity of the central star can reduce the amount of hot water vapor by a factor of 20 relative to the case with zero X-ray luminosity. In our test runs we did not see such an effect, and we interpret this as (see also Meijerink et al. 2012) due to the fact that our parameterized model does not adjust the vertical structure accordingly when the heating rate is increased, which would otherwise decrease the opacity to the dissociating UV photons.

### 2.3.6. Energy Exchange by Gas-dust Collision

The energy exchange between gas and dust particles due to collisions can heat or cool the gas, depending on whether the gas temperature is lower or higher than the dust. The energy exchange per unit volume per unit time is (Hollenbach & McKee 1979)

$$\Lambda_{\text{gd}} = 2k_{\text{B}}(T_{\text{gas}} - T_{\text{dust}})v_{\text{T}}\sigma_{\text{d}}n_{\text{dust}}n_{\text{gas}}f_{\text{a}}, \quad (19)$$

where the factor two is due to the fact that more energetic particles collide with the dust grain more frequently,  $v_{\text{T}}$  is the thermal speed of gas particles (equation (3)),  $\sigma_{\text{d}}$  is the mean cross section of dust particles, and  $f_{\text{a}}$  is the accommodation coefficient, for which we take the expression from Hollenbach & McKee (1989)

$$f_{\text{a}} = 1 - 0.8e^{-75/T_{\text{gas}}}. \quad (20)$$

If more than one dust species exists, their contributions are added together. We take into account the possibility that one type of dust particle heats the gas while another cools the gas.

### 2.3.7. Other Heating and Cooling Mechanisms

**Heating by photodissociation of  $\text{H}_2$**  We use the formula from Tielens (2005)

$$\Lambda_{\text{ph},\text{H}_2} = 1.36 \times 10^{-23} G_0 n(\text{H}_2), \quad (21)$$

where the unit is  $\text{erg s}^{-1} \text{ cm}^{-3}$ .  $G_0$  is the local UV intensity with self-shielding and dust extinction taken into account.

**Heating by photodissociation of  $\text{H}_2\text{O}$  and OH** Their contributions to heating are calculated with

$$\begin{aligned} \Gamma_{\text{ph},\text{H}_2\text{O}} &= F_{\text{Ly}\alpha} \sigma_{\text{H}_2\text{O}} n(\text{H}_2\text{O}) E_{\text{H}_2\text{O}}, \\ \Gamma_{\text{ph},\text{OH}} &= F_{\text{Ly}\alpha} \sigma_{\text{OH}} n(\text{OH}) E_{\text{OH}}, \end{aligned} \quad (22)$$

where  $F_{\text{Ly}\alpha}$  is the local Ly  $\alpha$  number flux,  $\sigma$  is the photodissociation cross section, and we take  $E_{\text{H}_2\text{O}} = 8.1 \times 10^{-12} \text{ erg}$  and  $E_{\text{OH}} = 9.2 \times 10^{-12} \text{ erg}$ , obtained by subtracting from the Ly  $\alpha$  photon energy the enthalpy change of the two dissociation reactions.  $E_{\text{H}_2\text{O}}$  may overestimate the actual value by a factor of 2 – 4, since a portion of the absorbed energy can be used to excite the internal modes of OH (Mordaunt et al. 1994).

**Heating by ionization of atomic carbon** We use the formula from Tielens (2005)

$$\Gamma_{\text{ion},\text{C}} = 2.2 \times 10^{-22} G_0 n(\text{C}), \quad (23)$$

with unit  $\text{erg s}^{-1} \text{ cm}^{-3}$ .

**Cooling by electrons recombine with small dust grains** We use the analytical formula from (Bakes & Tielens 1994)

$$\begin{aligned} \Lambda_{\text{recom}} &= 3.49 \times 10^{-30} n_{\text{e}} n_{\text{H}} T^{0.944} \\ &\times \left( \frac{G_0 T^{1/2}}{n_{\text{e}}} \right)^{\beta}, \end{aligned} \quad (24)$$

with unit  $\text{erg s}^{-1} \text{ cm}^{-3}$ .  $\beta = 0.735/T^{0.068}$ . This cooling rate is reduced when dust is depleted.

**Cooling by the rotational transitions of  $\text{H}_2$ , and the rotational and vibrational transitions of CO and  $\text{H}_2\text{O}$**  We calculate these cooling rates using the interpolation tables from Neufeld & Kaufman (1993) and Neufeld et al.

(1995) rather than direct radiative transfer for the sake of speed. These tables were made based on the escape probability approximation, in which a velocity gradient is needed, for which we use the radial gradient of the orbital speed

$$dv/dr = \frac{1}{2} \left( \frac{GM}{r^3} \right)^{1/2},$$

though note that since the orbital velocity is perpendicular to the radial direction, the photons cannot easily escape in the radial direction, but rather at an angle with it.

**Heating and cooling by the vibrational transitions of  $H_2$ , and cooling by  $C^+$  and O emission** We use the analytical formulae from Röllig et al. (2006). The escape probability for the  $C^+$  and O lines are also calculated based on the radial gradient of the orbital speed and the local velocity dispersion.

**Cooling by Ly  $\alpha$  emission, free-bound, and free-free emissions** They are usually not important for our purpose. We include them for completeness, using the formulae in Tielens (2005) and Draine (2010).

## 2.4. Disk Structure

We assume that the disk is static in the vertical direction and is in Keplerian rotation in the azimuthal direction (only needed for the line radiative transfer). The axisymmetric disk density structure we use takes the following parameterized form in cylindrical coordinates  $(r, z)$  (Lynden-Bell & Pringle 1974; Hartmann et al. 1998; Andrews et al. 2009; Cleeves et al. 2013)

$$\rho(r, z) = \frac{\Sigma}{\sqrt{2\pi}h} \exp \left[ -\frac{1}{2} \left( \frac{z}{h} \right)^2 \right], \quad (25)$$

where

$$\Sigma(r) = \Sigma_c \left( \frac{r}{r_c} \right)^{-\gamma} \exp \left[ -\left( \frac{r}{r_c} \right)^{2-\gamma} \right], \quad (26)$$

$$h = h_c \left( \frac{r}{r_c} \right)^\psi.$$

The disk mass (gas or dust) is

$$M_{\text{disk}} = \int_{r_{\text{in}}}^{r_{\text{out}}} \Sigma \, 2\pi r dr$$

$$= \frac{2}{2-\gamma} \pi r_c^2 \Sigma_c \left[ e^{-\left( \frac{r_{\text{in}}}{r_c} \right)^{2-\gamma}} - e^{-\left( \frac{r_{\text{out}}}{r_c} \right)^{2-\gamma}} \right]. \quad (27)$$

A list of the parameters involved and their meanings are in Table 2. Note that  $\Sigma_c$  is not included as an independent parameter since it can be calculated from equation (27). Also note that the gas and dust components of the disk can each have a different set of values for these parameters.

## 3. Results

### 3.1. A Fiducial Model

We first show a fiducial model with stellar and disk parameters listed in Table 2. The disk is assumed to have an inner hole with a sharp edge. Except for the radius of this edge, which is set to 1 AU here, those parameters are set to mimic the transition disk TW Hya as derived by Calvet et al. (2002). The input stellar UV spectrum (including the Ly  $\alpha$  line emission) is the observed spectrum of TW Hya (Herczeg et al. 2002, 2004). We did not take into account the possible UV variability. For the initial chemical composition, we assume hydrogen is in  $H_2$ , carbon is in gas phase CO, and oxygen not in CO is in water ice, while all the other elements are in atomic form. We assume two types of dust grains, each with a MRN (Mathis-Rumpl-Nordsieck) size distribution (Mathis et al. 1977). The two dust components are assumed to be spatially coexistent in this fiducial model. The larger population has  $r_{\text{min}} = 1 \mu\text{m}$  and  $r_{\text{max}} = 100 \mu\text{m}$ , with a dust-to-gas mass ratio of 0.01, while the smaller population has  $r_{\text{min}} = 0.01 \mu\text{m}$  and  $r_{\text{max}} = 1 \mu\text{m}$ , with a dust-to-gas mass ratio of  $2 \times 10^{-5}$ . Larger values for  $r_{\text{max}}$  of the big grains has been used in the literature for fitting the disk spectral energy distribution. However, the chemical processes mainly depends on the total available dust grain surface area, which is more sensitive to the assigned overall mass fractions of the small and big grains than the value of  $r_{\text{max}}$ . The dust material is assumed to be a 7 : 3 mixture of “smoothed UV astronomical silicate” and graphite. The optical parameters of the dust are taken from the website



Table 1: Initial chemical composition, relative to the total number density of hydrogen nuclei.  $a(b) \equiv a \times 10^b$ .

Species	Abundance
H <sub>2</sub>	0.5
He	0.09
CO	1.4(−4)
N	7.5(−5)
H <sub>2</sub> O (ice)	1.8(−4)
S	8(−8)
Si <sup>+</sup>	8(−9)
Na <sup>+</sup>	2(−8)
Mg <sup>+</sup>	7(−9)
Fe <sup>+</sup>	3(−9)
P	3(−9)
F	2(−8)
Cl	4(−9)

Table 2: Major parameters in our model, and their fiducial values.

Stellar parameters	
$M_{\text{star}}$	Mass; $0.6 M_{\odot}$
$R_{\text{star}}$	Radius; $1 R_{\odot}$
$T_{\text{star}}$	Effective temperature; 4000 K
$L_{\text{star}}$	Total luminosity; $0.25 L_{\odot}$
$L_{\text{UV}}$	UV continuum luminosity; $0.02 L_{\odot}$
$L_{\text{Ly}\alpha}$	Ly $\alpha$ luminosity; $0.004 L_{\odot}$
$L_{\text{Xray}}$	X-ray luminosity; $0.001 L_{\odot}$
Disk parameters	
$r_{\text{in}}$	radius of the disk inner edge; 1 AU
$r_{\text{out}}$	radius of the disk outer edge; 140 AU
$M_{\text{disk}}$	disk gas mass; $0.05 M_{\odot}$
$M_{\text{dust}}$	disk dust mass; $0.01 M_{\text{disk}}$
$r_{\text{c}}$	a characteristic radius; 100 AU
$h_{\text{c}}$	scale height at the characteristic radius; 10 AU
$\gamma$	power index for the disk surface density distribution; 1
$\psi$	power index for the scale height as a function of radius; 1
Other parameters	
$\alpha$	Turbulent viscosity parameter; 0.01
$\zeta$	Cosmic-ray ionization rate; $1.36 \times 10^{-17} \text{ s}^{-1}$
$G_{0,\text{ISM}}$	ISM UV field intensity; 1

of Bruce T. Draine<sup>4</sup> (Draine & Lee 1984; Laor & Draine 1993).

The input density structure, and the gas and dust temperature distribution obtained from radiative transfer and thermal balance calculation are shown in Figure 1. The dominant heating and cooling mechanisms are shown in Figure 2. In the disk upper layer heating is dominated by photoelectric effect, followed by H<sub>2</sub> formation heating in the photodissociation layer, and viscous heating in the deep region. Cooling is dominated by O I and C II lines in the upper layer, and by accommodation on the dust grains in the lower dense layers. Overall the distribution of the dominant heating and cooling mechanisms is similar to what is shown in Woitke et al. (2009a).

The gas phase H<sub>2</sub>O distribution is shown in Figure 3. Hot/warm water with temperature  $\gtrsim 200$  K is concentrated in a very small region close to the inner edge near the midplane, which can be seen clearly in the inset of this figure. The abundance of water vapor in this region is  $\gtrsim 2 \times 10^{-4}$ , which means essentially all the oxygen not in CO are found in H<sub>2</sub>O gas. The total warm water mass is  $7.7 \times 10^{26}$  g, which is equivalent to 560 times the mass of Earth oceans ( $M_{\text{ocean}}$ ), or  $\sim 0.1 M_{\text{Earth}}$ . Although the UV flux from the star is very strong ( $G_0 \sim 10^7$ ) at the disk inner edge, the destruction of water by UV radiation is completely quenched only slightly outward, due to the high density in this region. For example, with  $n_{\text{gas}} = 10^{14} \text{ cm}^{-3}$  and a dust-to-gas mass ratio of 0.01 (assuming  $1 \mu\text{m}$  for the dust grain radius), the attenuation length of the UV field is of the order of  $10^{-4}$  AU, which is too small to be seen in Figure 3. This explains why the warm water is located so close to the inner edge, as envisaged by Cleeves et al. (2011). Similar distributions can also be found in Woitke et al. (2009b), Aresu et al. (2011), Heinzeller et al. (2011), and Meijerink et al. (2012).

To understand the small extent of the warm water distribution, it suffices to know that, in a well shielded region, a high abundance of gas phase water can only be maintained if the dust temperature is higher than  $\sim 150$  K, the evaporation temperature of water, otherwise water will con-

<sup>4</sup><http://www.astro.princeton.edu/~draine/dust/dust.diel.html>

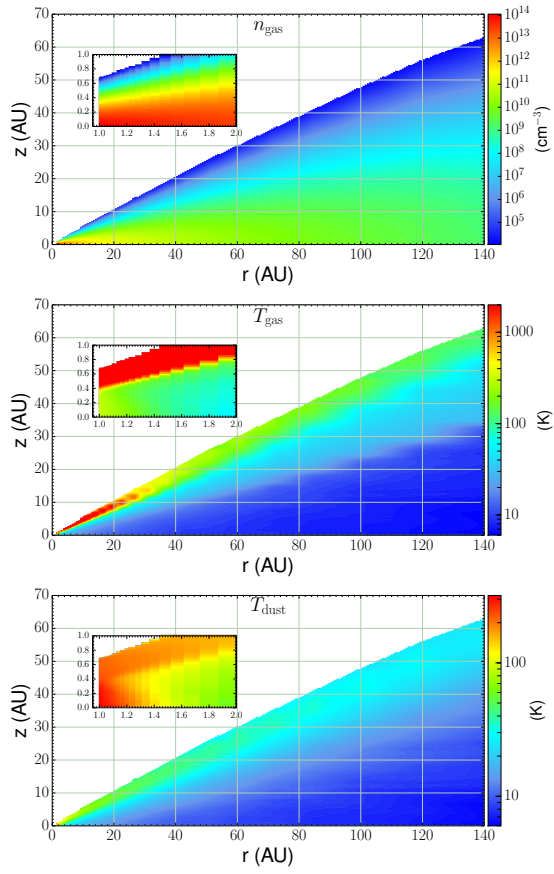


Fig. 1.— Distribution of gas density (top) used as input, and the calculated distribution of gas (middle) and dust (bottom) temperature in the fiducial model.

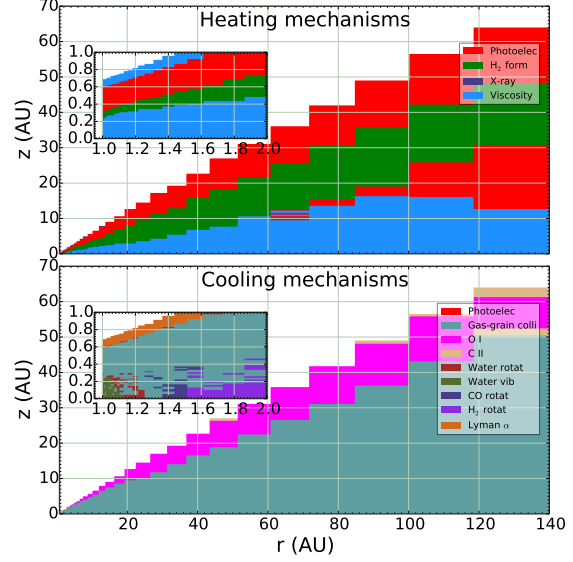


Fig. 2.— Dominant heating and cooling mechanisms in the disk. Note that at each location multiple heating/cooling mechanisms can be important, while only the one contributes most is drawn, which makes the distribution appear “spodic”.

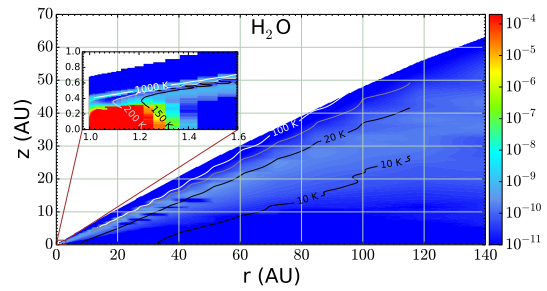


Fig. 3.— Distribution of water vapor in the disk, overlaid with contours of gas temperature. The inset show zoom-in view of the distribution close to the inner edge at 1 AU.

densate onto the dust grains to form ice. The radial temperature gradient close to the inner edge is very steep (see Figure 12), due to scattering and re-emission of radiation towards the disk upper and lower surface, which significantly reduces the amount of energy propagating radially outward. A semi-analytical account of the dust temperature profile in the midplane based on the diffusion approximation of radiative transfer is in Appendix A, where we will see that the dust temperature drops from  $>300$  K at the edge (1 AU) to  $100 - 150$  K at  $r = 1.5$  AU, beyond which water can only exist as ice unless some nonthermal desorption mechanisms come into play.

Besides the warm water close to the disk inner edge, there is also cold ( $\lesssim 50$  K) gas phase water in the higher layers throughout the disk (main panel of Figure 3). The dust temperature at places where this cold water resides in is well below the evaporation temperature of water, and here the gas phase water is formed from photodesorption of ice (Dominik et al. 2005). The total mass of this diffuse cold water vapor is  $\sim 0.006 M_{\text{ocean}}$ , but this value depends on the disk size. The overall water vapor mass budget as a function of gas temperature can be seen in the top panel of Figure 4, from which it is clear that a small amount of cold ( $< 80$  K) water is associated with reduced but nonzero UV field (indicated by the color scale of the histograms). We note that the total mass of cold water vapor from our model is close to what was derived by Hogerheijde et al. (2011). A small amount of water vapor can also be produced through the radiative association reaction  $\text{H} + \text{OH} \rightarrow \text{H}_2\text{O} + h\nu$  in the partially photodissociated layer in the outer disk (see also Kamp et al. 2013). Assuming the abundance of water vapor in the outer cold region is determined mainly by photodesorption, photodissociation, and adsorption, and assuming the dust grain is *fully* covered by water ice, we have

$$X[\text{H}_2\text{O}] = \frac{F_{\text{UV}}\sigma_d Y \eta_n}{F_{\text{UV}}\sigma' + n_{\text{H}}\eta_n\sigma_d v_{\text{T}}}, \quad (28)$$

where  $F_{\text{UV}}$  is the UV flux,  $\sigma_d$  is the dust grain cross section,  $Y$  is the photodesorption yield,  $\eta_n$  is the dust-to-gas number ratio,  $\sigma'$  is the water photodissociation cross section, and  $v_{\text{T}}$  is the thermal speed. As noted by Dominik et al. (2005) and Bergin et al. (2010), when adsorption is unimpor-

tant, the abundance of water vapor is independent of the UV flux,

$$X[\text{H}_2\text{O}] \simeq \frac{\sigma_d Y \eta_n}{\sigma'} \\ = 2.6 \times 10^{-9} \left( \frac{r_d}{0.1 \mu\text{m}} \right)^2 \left( \frac{\eta_n}{10^{-13}} \cdot \frac{Y}{10^{-3}} \right). \quad (29)$$

Deeper into the disk, the density becomes higher and the UV flux becomes weaker, and equation (29) will overestimate the water vapor abundance with respect to equation (28).

Also seen in Figure 4 is the existence of a small amount of hot water vapor ( $\gtrsim 300$  K), which is similar to the result of Woitke et al. (2009b). Except for the region close to the inner wall, where the dust temperature is higher than 300 K, the hot water vapor mainly exists in the upper layer of the disk with  $r \lesssim 30$  AU, where the density is low enough that the cooling by accommodation on dust grains is ineffective. The abundance of hot water in such region is  $\sim 10^{-10}$ , determined by the balance between photodissociation and warm neutral chemistry (see Woitke et al. 2009b; see also Appendix B).

In this section we have seen that the water budget is controlled by a few mechanisms: dissociation by UV photons, adsorption onto dust grains, and the shielding by dust (and possibly self-shielding). Warm water will be preserved in the gas phase if there is enough shielding while keeping the dust temperature higher than the water condensation point. In the next sections we will discuss their roles in more detail.

### 3.2. Effect of Disk Morphology

We have assumed a razor sharp inner edge in the fiducial model, which gives a well confined distribution of warm water close to the inner edge. We also run a test model with a “softer” inner edge, namely, we include an exponential taper so that the surface density profile becomes

$$\Sigma'(r) = \Sigma(r)e^{(r-r_0)/r_s}, \text{ if } r < r_0, \quad (30)$$

where  $\Sigma(r)$  is defined in equation (26), and  $r_0$  and  $r_s$  are the taper parameters. In the test model we let  $r_{\text{in}} = 0.5$  AU,  $r_0 = 2$  AU, and  $r_s = 0.2$  AU, while other parameters are the same as the fiducial model. As shown in the top panel of Figure 5, warm water in this test model is confined

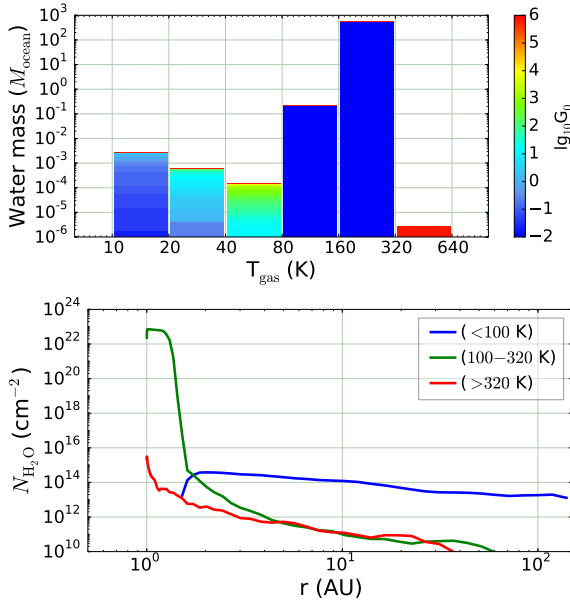


Fig. 4.— Top: water vapor mass in each logarithmic temperature bin in the fiducial model. The color scale indicates the UV intensity ( $G_0$ ) of the disk locations falling into each bin. Bottom: radial profile of the vertically integrated column density of water vapor in different temperature ranges.

in a small region around 1 AU, instead of being close to the edge at 0.5 AU, simply because the dust shielding only becomes important at  $\sim 1$  AU due to the reduced density near the inner edge. Further out from  $\sim 1.5$  AU the dust temperature becomes low enough for water to condense out. In this test case the total mass of warm water is very small, only  $\sim 0.8 M_{\text{ocean}}$ . There are two reasons for this: the tapered region has much smaller density (hence less mass) than the fiducial one, and the dust shielding in the vertical direction is also reduced (hence smaller volume for water to reside in). The column density of water vapor has a peak value of a few times  $10^{19} \text{ cm}^{-2}$  at  $r \simeq 1$  AU, with gas temperature  $\gtrsim 400$  K, which are similar to the fitting results of Salyk et al. (2011). For our model to be more close to reality, we will need to solve the disk physical structure self-consistently in a way similar to, e.g., Nomura (2002) or Woitke et al. (2009a), and this will be part of our future study.

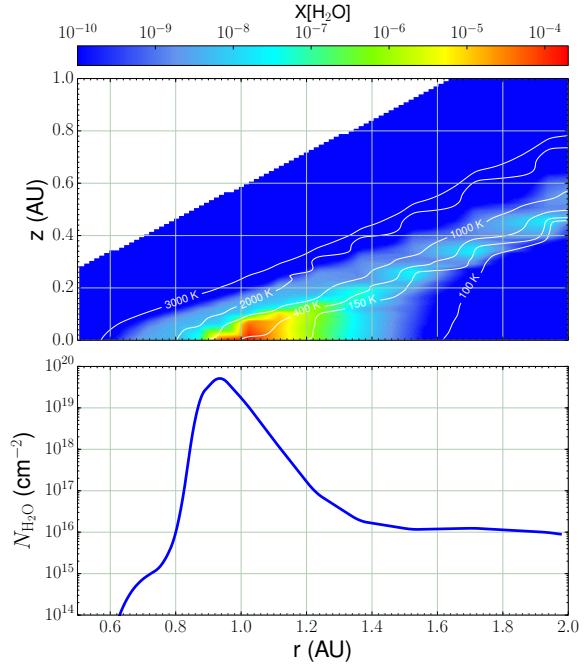


Fig. 5.— Top: distribution of water vapor in the inner disk, overlaid with contours of gas temperature. The disk inner edge is at 0.5 AU, with an exponential taper starting inward from 2 AU. Bottom: radial profile of water vapor column density.

### 3.3. Distribution of Warm Water as a Function of the Size of the Disk Inner Edge

The size of the inner hole of a protoplanetary disk may evolve as a result of material exhaustion due to photo-evaporation (Gorti & Hollenbach 2009; Owen et al. 2010), or accretion onto the central star or onto the forming planets. Since the warm water is concentrated close to the inner wall as seen in the previous section, we expect the amount of warm water vapor will also evolve as the inner hole expands.

We run a set of models with all the parameters except  $r_{\text{in}}$  taking the same value as in the fiducial model. The mass of water as a function of  $r_{\text{in}}$  is shown in the top panel of Figure 6. As expected, the warm water mass generally decreases as  $r_{\text{in}}$  increases. For  $r_{\text{in}} > 3.5$  AU, the amount of warm water vapor becomes very small because with a central star with bolometric luminosity of  $0.25 L_{\odot}$ , the temperature of the disk wall at 3.5 AU is  $\sim 170$  K (taking into account the re-absorption of the radiation emitted by the wall), only marginally higher than the water condensation temperature, hence warm water vapor can only exist in a thin skin of the inner wall.

The bottom panel of Figure 6 shows the vertical column density of water for  $r_{\text{in}}$  from 1 to 4 AU. The distribution of water vapor in the inner disk with column densities  $10^{19} - 10^{22} \text{ cm}^{-2}$  is consistent with the observations of Salyk et al. (2011), though the column densities they derived are mostly in a lower  $10^{18} - 10^{19} \text{ cm}^{-2}$  range. The water abundance is ultimately limited from above by the total amount of oxygen available. The narrow rings of water vapor with width  $\sim 0.2$  AU resembles what was found by Zhang et al. (2013), though for TW Hya, they apparently found a much higher column density ( $\sim 10^{22} \text{ cm}^{-2}$ , see their Figure 4) compared with  $10^{19} \text{ cm}^{-2}$  for the  $r_{\text{in}} = 4$  AU case in Figure 6. One simple way to get a higher column density from our model is to assume a higher surface density at the inner edge, though in our present model the surface density at the edge is already high ( $\sim 600 \text{ g cm}^{-2}$ ). One could in principle get a higher oxygen abundance (hence higher water column) relative to hydrogen if the latter has been photo-evaporated, without letting the surface density too high. Another pos-

sibility to increase the water abundance is related to the details of water adsorption and evaporation (onto and from the dust grains). Since the dust temperature at 4 AU is low ( $\sim 160$  K), water starts to condense out. The exact temperature for this to happen depends on the dust properties. We have assumed a water desorption energy of 5700 K (Fraser et al. 2001). Lowering this value will release more water into the gas phase. For example, as seen in the gray curve in the bottom panel of Figure 6, reducing it to 5000 K in a test run gives a peak water vapor column density of  $10^{21} \text{ cm}^{-2}$ . The desorption energy cannot be too low ( $\lesssim 4000$  K) either, because that will tend to overproduce gaseous water, as seen in the black curve in Figure 6. The adsorption and desorption dynamics of dust grains is a complicated issue, which involves the chemical composition, morphology, as well as crystalline structure of the ice, which themselves are related to their history of formation. The value of 5700 K is appropriate for high density amorphous water ice. Mixing with CO and  $\text{CO}_2$  ice (Tielens et al. 1991; Pontoppidan et al. 2008) can reduce the desorption energy of water due to weaker bonding (Cuppen & Herbst 2007), though this is not supposed to happen close to the inner edge of the disk, where CO should be mainly in gas phase. Finally, we must caution that potential degeneracy in parametric fitting of the molecular abundance distribution may render the above comparison premature.

### 3.4. The Effect of Stellar Luminosity

A more luminous central star can warm up the disk, which tends to have more water molecules released into the gas phase, at the same time it also emits more UV photons that can dissociate water molecules (though note that for young stars the UV photons are mainly produced nonthermally by magnetospheric accretion). To explore how the stellar luminosity affect the water distribution, we take a very simple approach by running a set of models with different effective temperature for the central star, assuming the stellar emission to be blackbody without any excess, while keeping all the other parameters the same as in the fiducial model. The mass of warm water vapor as a function of stellar temperature can be seen in the top panel of Figure 7, which shows that the warm water mass increases almost linearly with stellar tem-

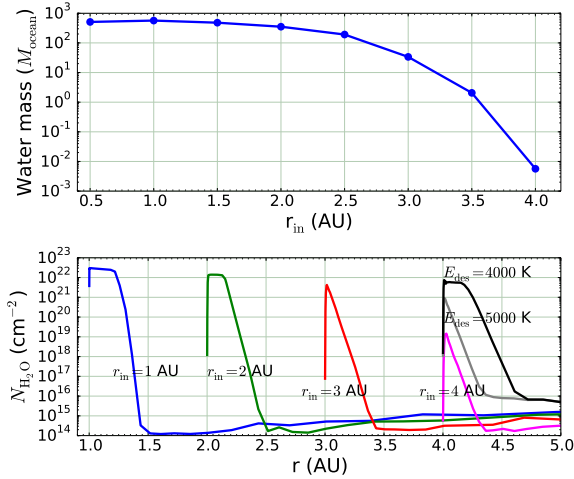


Fig. 6.— Top: Total mass of warm water (the unit is the mass of Earth ocean =  $1.4 \times 10^{24}$  g) as a function of the size of the disk inner edge. Bottom: Vertically integrated column density of water vapor for different disk models with  $r_{\text{in}}$  from 1 AU to 4 AU. The gray and black curves show test runs with the desorption energy of water set to 5000 K and 4000 K, respectively, while all the other curves are obtained with 5700 K.

perature. The reason is that in our model a higher stellar luminosity increases the overall temperature of the entire disk. The higher dissociating photon flux associated with a higher  $T_{\text{eff}}$  does not necessarily reduce the water content, because UV photons are readily shielded by the dust, and get converted into photons with lower frequency and no dissociating capability and diffuse into the disk to warm up the dust and gas. The column density profile for different stellar temperatures can be seen in the bottom panel of Figure 7. Higher stellar temperature leads to a wider profile, while the peak column densities are identical, since it is limited by the surface density. Admittedly, our treatment here is simplistic. In reality, a higher overall temperature would “blow up” the disk, reducing the opacity and letting the UV photons penetrate deeper into the disk to dissociate the water molecules, at the same time more water molecules might be liberated into the gas phase due to higher flux of desorbing UV photons.

To see the effect of assuming the stellar spectrum to be a blackbody, Figure 8 shows the column density profile of water vapor in different

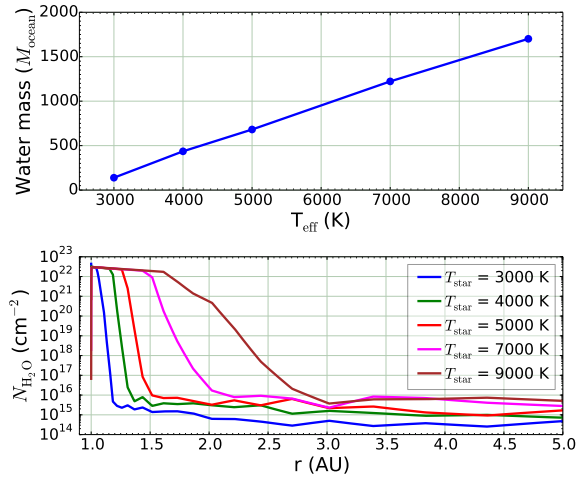


Fig. 7.— Top: Total mass of warm water as a function of the stellar temperature. The stellar spectrum is assumed to be blackbody. The inner edge is at  $r = 1$  AU. Bottom: Vertically integrated column density of water vapor for different assumed stellar temperatures.

temperature ranges with (solid line) or without (dashed line) UV excess in the input stellar spectrum, where the stellar temperature is 4000 K and the UV excess is taken to be the same as in the fiducial model. Although a UV excess slightly reduces the column density of the (300 – 1000) K component, it also increases the column density of the tenuous hot ( $T > 1000$  K) component, for which UV radiation is the major heating source (through photoelectric effect,  $\text{H}_2$  photodissociation,  $\text{H}_2$  vibrational excitation, etc.).

### 3.5. The Effect of Dust Settling

As the disk evolves, dust grains coagulate and grow to larger sizes, and gradually settle down to the midplane (and finally get assembled into forming planets or accreted into the star), leaving less dust in the bulk, and the dust grains that are left at higher altitudes will preferentially have a smaller size than those close to the midplane (but may still be larger than the ISM dust). Our model does not yet contain a self-consistent prescription for dust growth and settling (see, e.g., Dullemond & Dominik 2004b; Dullemond & Spruit 2005), so we simulate the effect of dust settling in a parameterization manner in two ways. The first is to re-

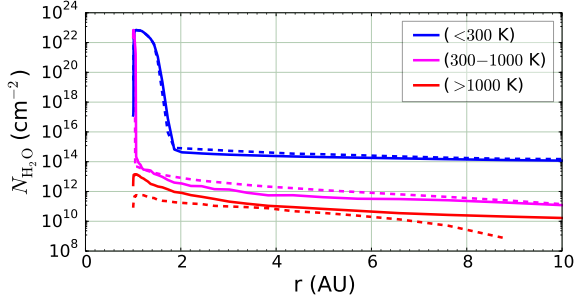


Fig. 8.— Column density profile of water vapor in three different temperature ranges, for a blackbody stellar spectrum ( $T_{\text{eff}} = 4000$  K, dashed lines), and for a stellar spectrum with UV excess (solid line).

duce the overall dust mass of the disk, while keeping the dust-to-gas mass ratio equal the fiducial value over the whole disk; the second is to reduce the scale height of the larger grains, keeping a population of small grains well-mixed with gas, while the overall dust-to-gas mass ratio stays the same as in the fiducial model.

The resulting warm water distribution as a function of dust-to-gas mass ratio and of the dust scale height can be seen in Figure 9 and Figure 10. The general trend is that less dust present in the bulk of the disk means less warm water vapor. The zoom-in plots in Figure 9 show that the size of the region containing high-abundance water vapor shrinks as the amount of dust is reduced. The main reason is that when dust is reduced, water is more susceptible to UV dissociation. For example, when the dust-to-gas mass ratio is reduced from 0.01 to  $10^{-4}$ , the UV field strength increase by more than a factor of  $10^3$  in the region where water would otherwise be formed and preserved in gas phase. The self-shielding of water only starts to work at a certain depth, depending on the density and UV intensity, but at such a depth the dust temperature may already drops to a level lower than the water condensation temperature. See the next section for further discussion on this. The reduction of dust does have a small positive effect on water vapor abundance: more water can be retained in the gas phase (if not photodissociated) due to less available adsorption area.

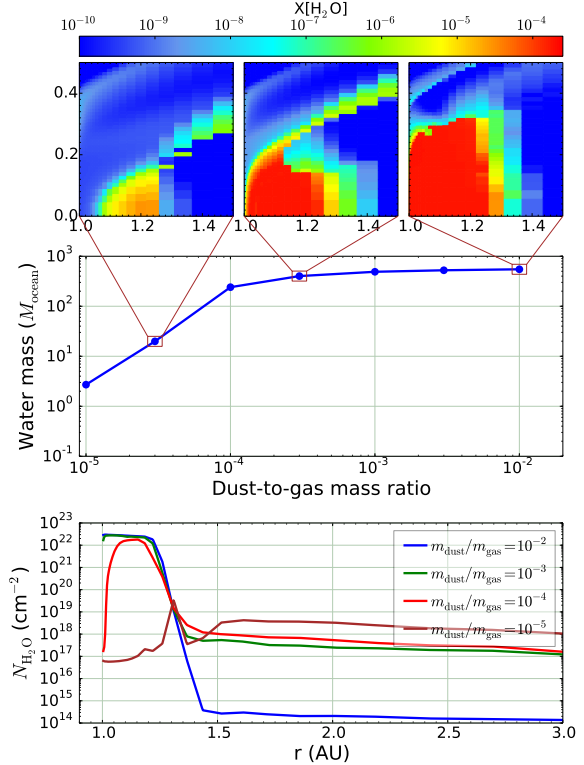


Fig. 9.— Water vapor properties for different dust-to-gas mass ratios. The top panel shows zoom-in view of water vapor distribution close to the inner edge (1 AU). The middle panel shows the total water vapor mass as a function of dust-to-gas mass ratio. The bottom panel shows the vertically integrated water vapor column density as a function of radius for different dust-to-gas mass ratios.

### 3.6. How Important is Water Self-shielding?

The self-shielding of water can be calculated with

$$f_{\text{sh},\text{H}_2\text{O}} = e^{-\sigma_{\text{H}_2\text{O}} N_{\text{H}_2\text{O}}}, \quad (31)$$

where  $\sigma_{\text{H}_2\text{O}}$  is the photodissociation cross section of water, which is  $1.2 \times 10^{-17} \text{ cm}^{-2}$  at the frequency of Ly  $\alpha$  (van Dishoeck et al. 2006). The dust shielding factor can be calculated with

$$f_{\text{sh},\text{dust}} = e^{-\sigma_{\text{d}} N_{\text{d}}}. \quad (32)$$

For a silicate grain with radius of  $1 \mu\text{m}$ , the absorption cross section at  $\lambda \sim 0.1 \mu\text{m}$  is about the same as the geometric cross section, hence we may have

$$\frac{\sigma_{\text{H}_2\text{O}} N_{\text{H}_2\text{O}}}{\sigma_{\text{d}} N_{\text{d}}} \simeq 40 \left[ \frac{X(\text{H}_2\text{O})}{2 \times 10^{-4}} \right] \left[ \frac{0.01}{\eta} \right] \left[ \frac{r_{\text{d}}}{1 \mu\text{m}} \right], \quad (33)$$

where  $\eta$  is the dust-to-gas mass ratio. Hence the absorption due to water can be dominant over dust if water is present in gas phase at its highest possible abundance, as shown by Bethell & Bergin (2009), which is also noted in Ádámkóvics et al. (2014).

However, we have seen in the previous section that when the dust is settled or reduced, the amount of water that is present is also reduced. This is because the abundance of  $\text{H}_2$  will be reduced due to the enhanced UV field and the fact that less dust surface area is available for its formation when dust is reduced ( $\text{H}_2$  can shield itself but nevertheless it needs dust surface to form), which will limit the formation of  $\text{H}_2\text{O}$  from the  $\text{O} \xrightarrow{\text{H}_2} \text{OH} \xrightarrow{\text{H}_2} \text{H}_2\text{O}$  chain (Ádámkóvics et al. 2014). Also of importance is that even if  $\text{H}_2$  is well shielded, CO may still be dissociated because its self-shielding is not as efficient. The produced C atoms can be an important competitor to the above chain to form water. When the gas becomes well-shielded by the dust,  $\text{H}_2$  becomes the dominant hydrogen bearer and carbon exists as CO, and  $\text{H}_2\text{O}$  can be formed and kept in the gas phase if the dust temperature is higher than the water condensation temperature. Actually, in a few test runs in which we turn off the self-shielding of  $\text{H}_2\text{O}$  in the radiative transfer or we assume all the oxygen not in CO is in gas phase (instead of ice) water for the initial chemical composition, no significant changes in the resulting water vapor mass can be

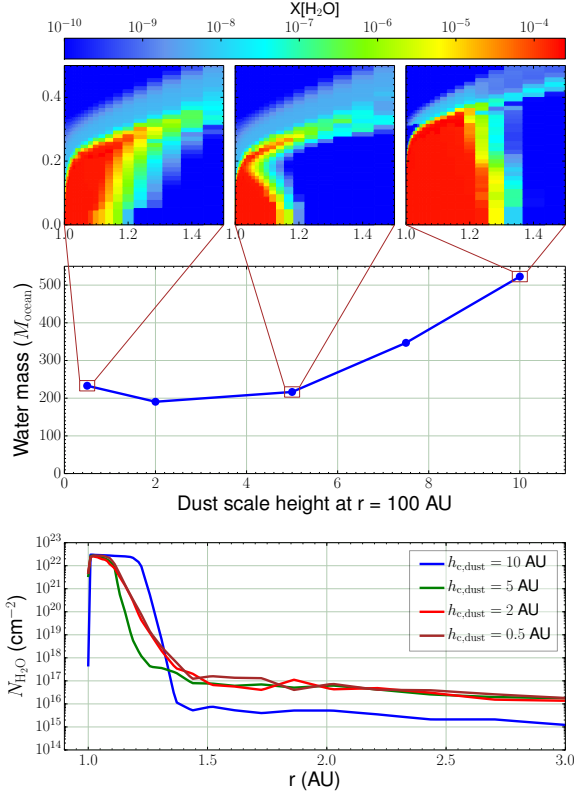


Fig. 10.— Similar to Figure 9, except for different dust scale heights (evaluated at  $r = 100 \text{ AU}$ ) for the larger dust grains. A population of small dust grains are always present in these models.



seen, though some small differences are indeed noticeable (see the next paragraph). Hence we may say that the self-shielding of water might be important but only in regions with rather special settings with regard to density structure, UV intensity, and dust abundance. Appendix B contains an approximate semi-analytical account similar to Bethell & Bergin (2009) for the role of water self-shielding.

The role of water self-shielding can also be checked from the output of our code. As already noted in section 2.1, our models work in an iterative manner. For iteration 0, the initial run, only dust absorption and scattering are included, while water absorption and atomic hydrogen scattering are *not* included in the radiative transfer. The radiative transfer outputs the distribution of dust temperature and radiation intensity over the whole disk, which is used in the chemical and thermal calculations. The updated chemical composition, specifically, the distribution of H and H<sub>2</sub>O, are used in the radiative transfer in the next iteration. This process goes on until the abundance distribution of major species (such as H, H<sub>2</sub>, CO, H<sub>2</sub>O) do not vary appreciably, though the randomness inherited from the Monte Carlo radiative transfer makes convergence in the usual sense difficult to achieve. Figure 11 shows changes in the radial water vapor abundance profiles at different vertical height as the iteration goes on. The dust-to-gas mass ratio is set to  $10^{-4}$ , and all the rest parameters are the same as the fiducial model. A close look at this figure shows that the curves for second and third iterations extend inward towards the central star relative to the curve of the first iteration, due to the self-shielding of water. For the midplane where the gas density is very high ( $10^{14} \text{ cm}^{-3}$ ), the relative shift is rather small and almost unnoticeable in the figure. For  $z = 0.1$  and  $0.15 \text{ AU}$  the effect is more obvious, and the peak abundance of water vapor is also raised by one order of magnitude, similar to what was found by Bethell & Bergin (2009, supporting online material). Higher in the disk atmosphere, with  $z = 0.2 \text{ AU}$ , where the density drops to about  $10^{13} \text{ cm}^{-3}$ , no relative shift can be noticed among different iterations. As calculated semi-analytically in Appendix B (Figure 14), with a density of  $10^{13} \text{ cm}^{-3}$ , a dust-to-gas mass ratio of  $10^{-4}$ , and a strong UV field, the depth for water

to be shielded is  $\sim 0.5 \text{ AU}$ . But at depth  $0.5 \text{ AU}$  into the disk the dust temperature will be just low enough (see Figure 1, or maybe more clearly, Figure 12) for water to condense out, and then the water vapor abundance will be determined by photo-desorption.

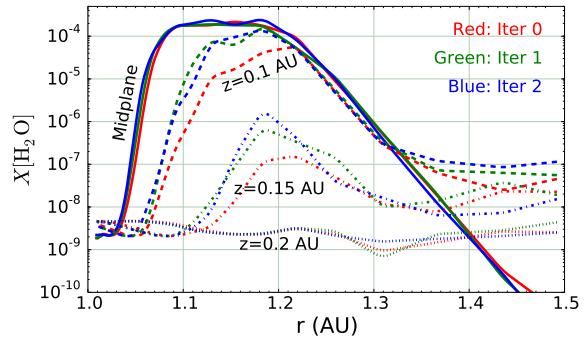


Fig. 11.— Changes in the radial water vapor abundance profile at different vertical height as the iteration proceeds.

#### 4. Discussion and Conclusions

We have modeled the formation of warm water vapor in protoplanetary disks with a comprehensive model. The radiative transfer of UV continuum and Ly  $\alpha$  photons and the associated heating of dust grains are calculated with a Monte Carlo method. The density structure is described in a parameterized manner, and the gas temperature structure is solved based on the balance between heating and cooling mechanisms. The chemical evolution is followed for 1 Myr.

We find that warm water is mainly distributed in a small region close to the inner edge of the disk. The location and size of this region is determined by two factors: the attenuation of the dissociating UV photons by dust grains and water molecules, and the condensation of water onto dust grains when the dust temperature abruptly drops below  $\sim 150 \text{ K}$ . At high densities and if dust is not severely settled, the attenuation length is very short (see Appendix B), so water vapor can exist right next to the edge (Cleeves et al. 2011). The diffusion and escape of photons creates a steep temperature drop at the inner edge, which limits the size of the region in which warm water vapor resides. Assuming the same disk structure, a more

luminous central star leads to a wider region where gas phase water is found in abundance. As dust grows and gets settled to the midplane, the region containing warm water vapor also shrinks, though a significant amount of water vapor can still exist if a population of small dust grains remain in the bulk of the disk.

Observationally, the concentration of warm water vapor in the inner disk will produce a sharp ring structure, which is, in general, in agreement with analysis of water vapor emission. We do note that, specifically in the case of TW Hya, the column density of water vapor at  $\sim 4$  AU predicted by our model is lower than the best-fit value of Zhang et al. (2013) by three orders of magnitude, unless we use a desorption energy of water lower than what is experimentally determined. Also for TW Hya, the amount of diffuse cold water vapor produced by photodesorption in our model is close to the observed value of Hogerheijde et al. (2011). Whether the discrepancy (and agreement) here should be taken seriously can only be answered with detailed radiative transfer modeling based on the chemical structure, which will be the topic of a future paper.

It might be possible to use warm water vapor as a tracer of the kinetics of the inner disk, since it is concentrated in a small inner region (Pontoppidan et al. 2010a) at or close to where planets form. In the era of ALMA, it may also become possible to directly map the distribution of spectrally resolved lines of water vapor (or rather its isotopologue  $\text{H}_2^{18}\text{O}$  to avoid absorption from the telluric water line) in the inner region of nearby protoplanetary disks. For example, the  $4_{14} - 3_{21}$  line of  $\text{H}_2^{18}\text{O}$  at 390.60776 GHz will become optically thick if  $N(\text{H}_2^{16}\text{O}) \gtrsim 2 \times 10^{19} \text{ cm}^{-2}$ , assuming a  $^{16}\text{O}/^{18}\text{O}$  ratio of 500 and  $T \gtrsim 300$  K. With the highest possible resolution of the full ALMA array at this wavelength ( $\sim 0.01''$ ), a warm water vapor ring with radius  $\sim 1$  AU in a protoplanetary disk 100 pc away is marginally resolvable.

In Appendix B we semi-analytically study the importance of the shielding due to water and OH. They can be important in some part of the parameter space (high density, low but nonzero dust-to-gas mass ratio, intermediate UV field), but their role is likely to be too subtle to be of paramount importance in generic settings.

We thank N. Calvet and L. Hartmann for useful discussions on radiative transfer and viscous heating. This work is supported by grant NNX12A193G from the NASA Origin of Solar Systems Program.

### A. Radial Temperature Profile Close to the Disk Inner Edge

When the medium is very opaque, the transfer of radiation can be approximated by a diffusion process, which gives the following equation for the temperature gradient

$$\frac{\partial T}{\partial r} = -\frac{3}{64\pi\sigma_{\text{SB}}} \frac{\kappa_{\text{R}}\rho l f}{r^2 T^3}. \quad (\text{A1})$$

This equation is a modified version of the one in Kippenhahn et al. (2012). In the above equation,  $\sigma_{\text{SB}}$  is the Stefan-Boltzmann constant,  $\kappa_{\text{R}}$  is the Rosseland mean opacity,  $\rho$  is the density,  $l$  is the stellar luminosity, and  $f$  is a function of  $r$  to account for the “leakage” of radiation from the upper and lower surfaces of the disk. Without the  $f$  factor, the equation only applies for spherical geometry. At low temperature,  $\kappa_{\text{R}}$  is roughly proportional to  $T^2$  (Krügel 2008). For a disk model with  $\Sigma(r) \propto r^{-1}$  and  $h \propto r$ , we have  $\rho \propto r^{-2}$ . For the function  $f$ , we may qualitatively parameterize it as

$$f(r) = \frac{ar^2}{(a+1)r^2 - r_{\text{in}}^2}, \quad (\text{A2})$$

where  $r_{\text{in}}$  is the disk inner radius, and the empirical parameter  $a \ll 1$  is roughly the fraction of energy transported radially outward through the disk edge (rather than through the upper and lower surface). We thus have

$$\frac{\partial T}{\partial r} \propto -T^{-1}r^{-4}f(r). \quad (\text{A3})$$

Here we are only concerned with the inner region (and the approximation we use here does not apply to the outer region anyway), so we may assume

$$x \equiv (r - r_{\text{in}})/r_{\text{in}} \ll 1.$$

An approximate solution in this regime is

$$T = T_{\text{in}} \left[ 1 - \frac{3a}{16} \frac{r_{\text{in}}}{l_{\text{PH}}} \ln \left( 1 + \frac{2}{a} x \right) \right]^{1/2}, \quad (\text{A4})$$

where  $T_{\text{in}}$  is the dust temperature right at the inner edge, and  $l_{\text{PH}} \equiv (\kappa_{\text{R}}\rho)^{-1}$  is the mean free path of photons (emitted by dust of temperature  $\sim T_{\text{in}}$ ). For  $T_{\text{in}} = 300$  K and  $n = 10^{14} \text{ cm}^{-3}$ , using the calculated Rosseland opacity from Semenov et al. (2003), we have  $l_{\text{PH}} \sim 0.01$  AU. Take  $r_{\text{in}} = 1$  AU and  $a = 0.01$ , we then have

$$T = T_{\text{in}} [1 - 0.2 \ln(1 + 200x)]^{1/2},$$

which means that an outward shift of only 0.2 AU from the inner edge can reduce the temperature by half. A fitting based on the analytical integration of equation (A3) to the midplane dust temperature profile (calculated from Monte Carlo simulation) of the inner disk is shown in Figure 12, which is not perfect but captures the major trend.

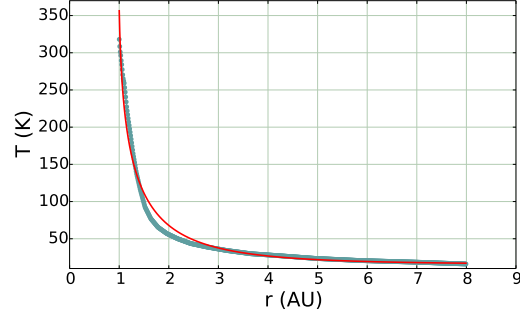


Fig. 12.— Mid-plane temperature of the inner disk as a function of radius, overlapped with an analytical fitting (red thin line).

### B. An Analytical Treatment for Warm Water Formation under Photodissociation

Here we present an approximate analytical treatment of water formation with warm neutral chemistry under the effect of UV photodissociation. This treatment is very similar to the one in Bethell & Bergin (2009), except that here we include the formation and photodissociation of  $\text{H}_2$ , and the geometry we assume is much simpler. As sketched in Figure 13, we consider a uniform and isothermal slab of gas and dust irradiated by external UV field. To put in context, this slab may be viewed as one horizontal slice of the inner disk, and the irradiation comes from the central star. The goal here is *not* to imitate a realistic circumstellar disk, but rather to see to what extent is water (and OH) shielding important.

We consider water formation through hot neu-

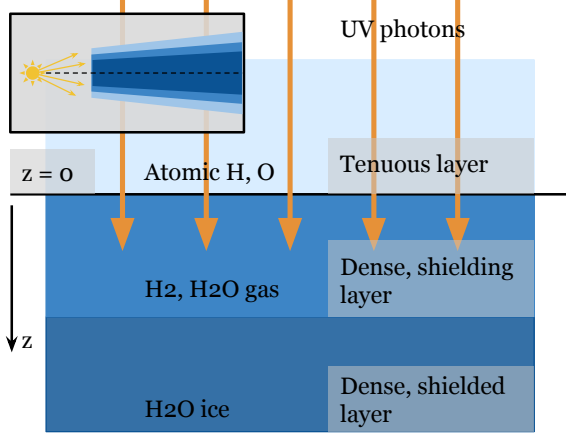
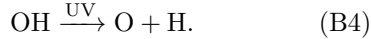
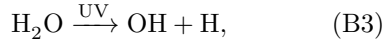
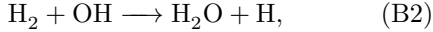
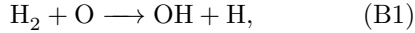


Fig. 13.— Sketch of the analytical toy model. Here we are mainly concerned with the tenuous layer and the shielding layer. The small inset shows the context where this toy model may be applied.

tral chemistry and destruction by UV photons:



For simplicity competitive channels such as  $\text{C} + \text{OH} \longrightarrow \text{CO} + \text{H}$  and  $\text{O} + \text{OH} \longrightarrow \text{O}_2 + \text{H}$  are omitted. They can be important in regions where CO and  $\text{H}_2$  are partially dissociated or where the temperature is low ( $\lesssim 200$  K). The four reactions gives the following set of equations:

$$\partial_t n(\text{H}_2\text{O}) = -k_{\text{B3}}n(\text{H}_2\text{O}) + k_{\text{B2}}n(\text{H}_2)n(\text{OH}), \quad (\text{B5})$$

$$\partial_t n(\text{OH}) = -k_{\text{B4}}n(\text{OH}) - k_{\text{B2}}n(\text{H}_2)n(\text{OH}), \quad (\text{B6})$$

$$+ k_{\text{B1}}n(\text{H}_2)n(\text{O}) + k_{\text{B3}}n(\text{H}_2\text{O}), \quad (\text{B7})$$

$$\partial_t n(\text{O}) = -k_{\text{B1}}n(\text{H}_2)n(\text{O}) + k_{\text{B4}}n(\text{OH}). \quad (\text{B8})$$

We further assume that oxygen is completely contained in the three species:

$$n(\text{H}_2\text{O}) + n(\text{OH}) + n(\text{O}) = n_{\text{O}}, \quad (\text{B9})$$

where  $n_{\text{O}}$  is the density of oxygen nucleus.

Assuming steady-state condition, we can readily solve the above equations to get

$$n(\text{OH}) = n(\text{H}_2\text{O}) \frac{k_{\text{B3}}}{k_{\text{B2}}n(\text{H}_2)}, \quad (\text{B10})$$

$$n(\text{O}) = n(\text{OH}) \frac{k_{\text{B4}}}{k_{\text{B1}}n(\text{H}_2)}, \quad (\text{B11})$$

$$n(\text{H}_2\text{O}) = \frac{n_{\text{O}}}{1 + \frac{k_{\text{B3}}}{k_{\text{B2}}n(\text{H}_2)} \left( 1 + \frac{k_{\text{B4}}}{k_{\text{B1}}n(\text{H}_2)} \right)}. \quad (\text{B12})$$

The above three relations hold at each point of the slab. Since the parameters  $n(\text{H}_2)$ ,  $k_{\text{B3}}$ , and  $k_{\text{B4}}$  in the right hand side may change with depth, so will the variables in the left hand side, which is what we will solve in the following.

At the present we are mainly concerned with the initial growth of  $n(\text{H}_2\text{O})$  as a function of  $z$ , so we can assume

$$\frac{k_{\text{B4}}}{k_{\text{B1}}n(\text{H}_2)} \gtrsim \frac{k_{\text{B3}}}{k_{\text{B2}}n(\text{H}_2)} \gg 1.$$

If this assumption does not hold, then we would already have  $n(\text{H}_2\text{O}) \sim n_{\text{O}}$ , and no further discussions are needed. Hence we may first approximate equation (B12) by

$$n(\text{H}_2\text{O}) = n_{\text{O}} \frac{k_{\text{B1}}k_{\text{B2}}n^2(\text{H}_2)}{k_{\text{B3}}k_{\text{B4}}} \quad (\text{B12}')$$

This will slightly *overestimate* the abundance of  $\text{H}_2\text{O}$ .

The photodissociation rate  $k_{\text{B3}}$  and  $k_{\text{B4}}$  can be written as

$$k_{\text{B3}} = k_{\text{B3},0} \exp[-\sigma_{\text{B3}}N(\text{H}_2\text{O}) - \sigma_{\text{B4}}N(\text{OH}) - \sigma_{\text{d}}N_{\text{d}}],$$

$$k_{\text{B4}} = k_{\text{B4},0} \exp[-\sigma_{\text{B3}}N(\text{H}_2\text{O}) - \sigma_{\text{B4}}N(\text{OH}) - \sigma_{\text{d}}N_{\text{d}}], \quad (\text{B13})$$

in which the self-shielding of water and OH and the shielding due to dust are included.  $k_{\text{B3},0}$  and  $k_{\text{B4},0}$  are the unshielded rate,  $\sigma_{\text{B3}}$  and  $\sigma_{\text{B4}}$  are the dissociation cross section of water and OH, and  $\sigma_{\text{d}}$  is the dust absorption cross section.  $N(\text{H}_2\text{O})$ ,  $N(\text{OH})$ , and  $N_{\text{d}}$  are the respective column densities.

Combining equation (B12') and equation (B13), we have

$$\sigma_{\text{B3}}N(\text{H}_2\text{O}) + \sigma_{\text{B4}}N(\text{OH}) + \sigma_{\text{d}}N_{\text{d}} = \frac{1}{2} \ln \left( \frac{n(\text{H}_2\text{O})k_{\text{B3},0}k_{\text{B4},0}}{n_{\text{O}}k_{\text{B1}}k_{\text{B2}}n^2(\text{H}_2)} \right) \quad (\text{B14})$$

Differentiating both sides with respect to  $z$  gives

$$\begin{aligned}
& \frac{1}{n(\text{H}_2\text{O})} \frac{d}{dz} n(\text{H}_2\text{O}) - \frac{2}{n(\text{H}_2)} \frac{d}{dz} n(\text{H}_2) \\
&= 2(\sigma_{\text{B}3} n(\text{H}_2\text{O}) + \sigma_{\text{B}4} n(\text{OH}) + \sigma_{\text{d}} n_{\text{d}}) \\
&= 2 \left[ \sigma_{\text{B}3} n(\text{H}_2\text{O}) \right. \\
&\quad + \sigma_{\text{B}4} \left( \frac{k_{\text{B}3,0} k_{\text{B}1} n_{\text{O}}}{k_{\text{B}4,0} k_{\text{B}2} n(\text{H}_2\text{O})} \right)^{1/2} n(\text{H}_2\text{O}) \\
&\quad \left. + \sigma_{\text{d}} n_{\text{d}} \right], \tag{B15}
\end{aligned}$$

where we have used equation (B10), (B13), and (B14), and have assumed temperature and density are constant.

Define  $x \equiv n(\text{H}_2\text{O})/n_{\text{O}}$ ,  $x_{\text{d}} \equiv n_{\text{d}}/n_{\text{O}}$ , we get

$$\begin{aligned}
\frac{d}{dz} x &= 2n_{\text{O}} \left[ \sigma_{\text{B}3} x^2 + \sigma_{\text{B}4} \left( \frac{k_{\text{B}3,0} k_{\text{B}1}}{k_{\text{B}4,0} k_{\text{B}2}} \right)^{1/2} x^{3/2} + \right. \\
&\quad \left. \sigma_{\text{d}} x_{\text{d}} x \right] + \frac{2x}{n(\text{H}_2)} \frac{d}{dz} n(\text{H}_2). \tag{B16}
\end{aligned}$$

This equation only works for  $x \ll 1$ .

The  $\text{H}_2$  abundance can be calculated by

$$n(\text{H}_2) = n_{\text{H}} \times \frac{n_{\text{d}} \tilde{\sigma}_{\text{d}} v_{\text{T}} / 2}{\xi + n_{\text{d}} \tilde{\sigma}_{\text{d}} v_{\text{T}}}, \tag{B17}$$

where  $\tilde{\sigma}_{\text{d}}$  is the dust particle cross section for adsorbing H atoms (to be distinguished from the cross section  $\sigma_{\text{d}}$  for absorbing UV photons),  $v_{\text{T}}$  is the average velocity of H atoms, and  $\xi$  is the total dissociation (photo + cosmic-ray) rate of  $\text{H}_2$ . In calculating  $\xi$  we take into account the dust attenuation and the  $\text{H}_2$  self-shielding. Since the self-shielding of  $\text{H}_2$  involves the column density of  $\text{H}_2$  (Draine & Bertoldi 1996), we first treat equation (B17) as a differential equation of  $N(\text{H}_2)$  since  $dN(\text{H}_2)/dz = n(\text{H}_2)$ , and after  $N(\text{H}_2)$  at depth  $z$  is solved, its value is feed back to equation (B17) to get  $n(\text{H}_2)$  at  $z$ . This is similar to Tielens (2005, p289).

When solving equation (B16) it is important to get the boundary value  $x|_{z=0}$  right. We calculate this value based on equation (B12), but corrected for the competitive reactions involving O and C, though these reactions are not included in the integration. In the calculation the dust property is

taken to be the same as in the fiducial model (Section 3.1). We adopt the following rate parameters:

$$\begin{aligned}
k_{\text{B}1} &= 3.14 \times 10^{-13} \left( \frac{T}{300} \right)^{2.7} e^{-3150/T} \text{ cm}^3 \text{ s}^{-1}, \\
k_{\text{B}2} &= 2.05 \times 10^{-12} \left( \frac{T}{300} \right)^{1.52} e^{-1736/T} \text{ cm}^3 \text{ s}^{-1}, \\
k_{\text{B}3,0} &= 1.2 \times 10^{-4} \left( \frac{F_{\text{Ly}\alpha}}{10^{13} \text{ cm}^{-2} \text{ s}^{-1}} \right) \text{ s}^{-1}, \\
k_{\text{B}4,0} &= 1.8 \times 10^{-5} \left( \frac{F_{\text{Ly}\alpha}}{10^{13} \text{ cm}^{-2} \text{ s}^{-1}} \right) \text{ s}^{-1}, \\
\sigma_{\text{B}3} &= 1.2 \times 10^{-17} \text{ cm}^2, \\
\sigma_{\text{B}4} &= 1.8 \times 10^{-18} \text{ cm}^2, \tag{B18}
\end{aligned}$$

where  $F_{\text{Ly}\alpha}$  is the number flux of Ly  $\alpha$  photons. We assume  $T = 300$  K.

The importance of the shielding due to  $\text{H}_2\text{O}$  and OH can be tested by considering the changes in the depth (we call it “shielding depth”) at which water reaches a “high” abundance, which we arbitrarily take to be 10% of the total available oxygen abundance. The shielding depth as a function of the dust-to-gas mass ratio is plotted in Figure 14 for different densities. The solid lines are for cases which include the shielding due to dust,  $\text{H}_2\text{O}$ , and OH, while the dashed lines are for cases in which the shielding due to  $\text{H}_2\text{O}$  and OH are turned off. Different panels have a different UV continuum and Ly  $\alpha$  intensity.

As can be seen in Figure 14, for lower densities ( $n_{\text{H}} = 10^{11} \text{ cm}^{-3}$ ) and strong UV fields, the shielding depth is rather large ( $\gtrsim 1$  AU) for normal or small dust-to-gas mass ratios, which indicates that in reality water cannot form through the hot neutral chemistry at such densities (if the UV radiation is as strong as we have assumed here), because at the calculated shielding depth the dust temperature might have decreased to the condensation temperature of water. Also can be seen is that the effect of turning-off the shielding due to water and OH is not significant for low densities, high dust-to-gas mass ratio, or strong UV fields, but becomes significant otherwise. For example, for  $n_{\text{H}} = 10^{14} \text{ cm}^{-3}$ , in the strong UV field case, when the dust-to-gas mass ratio is reduced to  $0.1 - 10^{-3}$  times the normal ISM value, turning off  $\text{H}_2\text{O}$  and OH shielding increases the shielding depth by a factor of a few to ten, while

in the weak UV field case the shielding depth can increase by more than two orders of magnitude. On the other hand, the shielding depths at such high densities are small anyway, hence the changes may not have obvious practical effects. For example, Figure 15 shows the radial water abundance profile at the midplane ( $n_{\text{H}} \sim 10^{14} \text{ cm}^{-3}$ ) for dust-to-gas mass ratio equal  $10^{-4}$ , with or without water shielding. Without water shielding the profile recedes slightly further away from the inner edge. With even smaller dust-to-gas mass ratio the distinction will be larger. However, as described above for the low density case, since the shielding depth increases as dust-to-gas mass ratio decreases, at some point the shielding depth will be large enough that the dust temperature drops below the water condensation temperature, and it becomes impossible to keep abundant water in the gas phase. In the extreme case, when there is no dust, then the problem becomes that  $\text{H}_2$  cannot be maintained (for  $G_0 = 10^7$  the photodissociation time scale of  $\text{H}_2$  is of the order of days) for water to form in the first place. Another issue is that, when the dust becomes optically thin, the dust temperature may also drop because less radiation can be trapped, which makes water more likely to condense out unless the total surface area of dust grains has been extremely reduced.

In the above discussions we did not include chemical reactions involving excited  $\text{H}_2$  molecules. UV radiation can excite  $\text{H}_2$  molecules to vibration levels with  $v > 0$ , which is capable of increasing the rate coefficients profoundly (Agúndez et al. 2010). However, the net effect depends on the abundance of excited  $\text{H}_2$ , which depends on the UV intensity and collisional deexcitation rates. For density higher than  $\sim 10^{11} \text{ cm}^{-3}$  and  $G_0 \sim 10^7$ , we estimate that the abundance of excited  $\text{H}_2$  will be too low to affect the discussion here.

As a side note regarding Figure 15, the fact that the depth at which the water abundance reaches higher than 10% of the total oxygen abundance is larger than what would be expected from the top panel of Figure 14 (0.05 AU versus 0.01 AU) is due to the activation of hot neutral chemistry that destroys water. Since the dust-to-gas mass ratio is much reduced, the accommodation cooling is not effective and the gas temperature can be much higher than the dust temperature ( $\sim 1500 \text{ K}$

versus  $\sim 200 \text{ K}$ ). At this temperature not only  $\text{H}_2\text{O}$  gets destroyed by reacting with H atoms,  $\text{H}_2$  is also reduced to a low abundance ( $\sim 0.01$ ) due to reaction with OH. A simple analytical model cannot easily capture all these features.

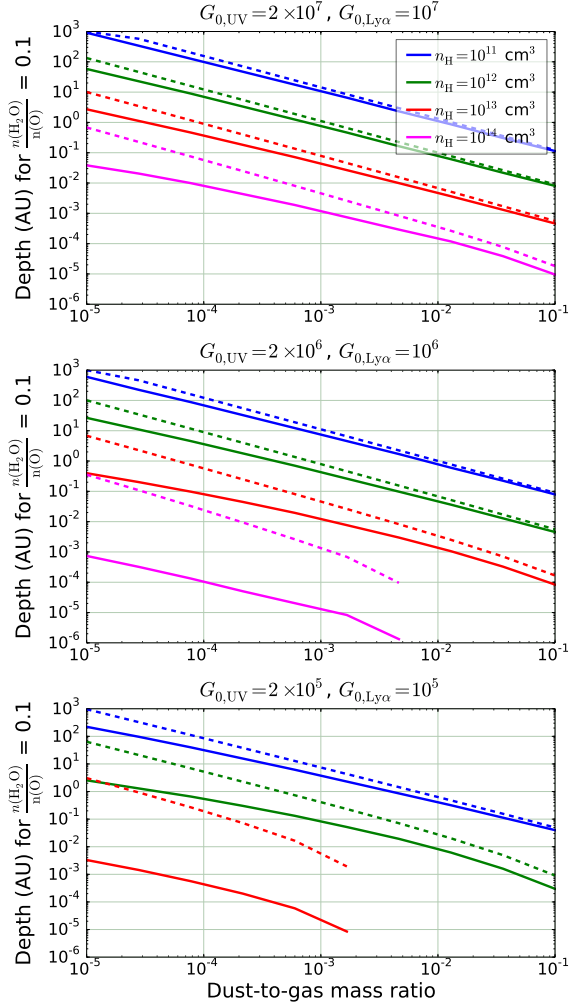


Fig. 14.— Shielding depth of  $\text{H}_2\text{O}$  (the depth at which  $n(\text{H}_2\text{O})$  reaches  $0.1n_{\text{O}}$ ) as a function of dust-to-gas mass ratio for different gas densities. The top panel has the strongest UV fields, and the bottom one has the weakest. The solid lines are for cases in which the shielding due to dust,  $\text{H}_2\text{O}$ , and  $\text{OH}$  are all considered, while the dashed lines are for cases in which only dust shielding is included. The magenta curves (for the  $n_{\text{H}} = 10^{14} \text{ cm}^{-3}$  case) are below the lower plotting range in the bottom panel.

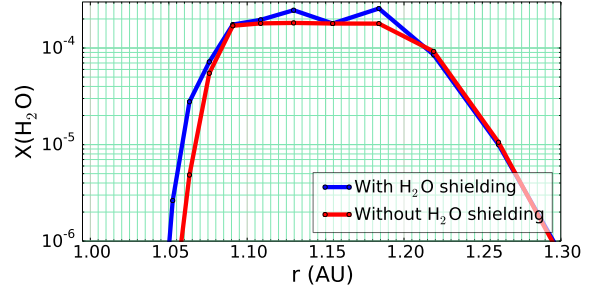


Fig. 15.— Midplane water abundance as a function of radius for two cases with or without the shielding due to  $\text{H}_2\text{O}$  included. The dust-to-gas mass ratio is  $10^{-4}$ . The disk inner edge is at 1 AU. Note that they are calculated from our full code, not from the simple semi-analytical model presented in this appendix, hence the shielding depths are not as shown in Figure 14.

## REFERENCES

- Ádámkóvics, M., Glassgold, A. E., & Najita, J. R. 2014, *ApJ*, 786, 135
- Agúndez, M., Goicoechea, J. R., Cernicharo, J., Faure, A., & Roueff, E. 2010, *ApJ*, 713, 662
- Albertsson, T., Semenov, D., & Henning, T. 2014, *ApJ*, 784, 39
- Andrews, S. M., Wilner, D. J., Hughes, A. M., Qi, C., & Dullemond, C. P. 2009, *ApJ*, 700, 1502
- Aresu, G., Kamp, I., Meijerink, R., et al. 2011, *A&A*, 526, A163
- Baes, M., Dejonghe, H., & Buyle, P. 2005, *A&A*, 432, 411
- Bai, X.-N., & Stone, J. M. 2011, *ApJ*, 736, 144
- Bakes, E. L. O., & Tielens, A. G. G. M. 1994, *ApJ*, 427, 822
- Bergin, E., Calvet, N., D'Alessio, P., & Herczeg, G. J. 2003, *ApJ*, 591, L159
- Bergin, E. A., Hogerheijde, M. R., Brinch, C., et al. 2010, *A&A*, 521, L33
- Bethell, T., & Bergin, E. 2009, *Science*, 326, 1675
- Bethell, T. J., & Bergin, E. A. 2011a, *ApJ*, 740, 7
- . 2011b, *ApJ*, 739, 78
- Binnewies, M., & Milke, E. 2002, *Thermochemical data of elements and compounds* (Wiley-VCH)
- Bjorkman, J. E., & Wood, K. 2001, *ApJ*, 554, 615
- Bruderer, S., Benz, A. O., Doty, S. D., van Dishoeck, E. F., & Bourke, T. L. 2009a, *ApJ*, 700, 872
- Bruderer, S., Doty, S. D., & Benz, A. O. 2009b, *ApJS*, 183, 179
- Bruderer, S., van Dishoeck, E. F., Doty, S. D., & Herczeg, G. J. 2012, *A&A*, 541, A91
- Calvet, N., D'Alessio, P., Hartmann, L., et al. 2002, *ApJ*, 568, 1008
- Carr, J. S., & Najita, J. R. 2008, *Science*, 319, 1504
- Carr, J. S., Tokunaga, A. T., & Najita, J. 2004, *ApJ*, 603, 213
- Cazaux, S., & Tielens, A. G. G. M. 2004, *ApJ*, 604, 222
- Cazaux, S. M., Caselli, P., Walmsley, M., & Tielens, A. G. G. M. 2005, in *IAU Symposium*, Vol. 231, *Astrochemistry: Recent Successes and Current Challenges*, ed. D. C. Lis, G. A. Blake, & E. Herbst, 325–336
- Chaabouni, H., Bergeron, H., Baouche, S., et al. 2012, *A&A*, 538, A128
- Cleeves, L. I., Adams, F. C., & Bergin, E. A. 2013, *ApJ*, 772, 5
- Cleeves, L. I., Bergin, E. A., Alexander, C. M. O., et al. 2014, submitted
- Cleeves, L. I., Bergin, E. A., Bethell, T. J., et al. 2011, *ApJ*, 743, L2
- Cuppen, H. M., & Herbst, E. 2007, *ApJ*, 668, 294
- Dalgarno, A., & Oppenheimer, M. 1974, *ApJ*, 192, 597
- Dominik, C., Ceccarelli, C., Hollenbach, D., & Kaufman, M. 2005, *ApJ*, 635, L85
- Doppmann, G. W., Najita, J. R., Carr, J. S., & Graham, J. R. 2011, *ApJ*, 738, 112
- Draine, B. 2010, *Physics of the Interstellar and Intergalactic Medium*, Princeton Series in Astrophysics (Princeton University Press)
- Draine, B. T., & Bertoldi, F. 1996, *ApJ*, 468, 269
- Draine, B. T., & Lee, H. M. 1984, *ApJ*, 285, 89
- Dullemond, C. P., & Dominik, C. 2004a, *A&A*, 417, 159
- . 2004b, *A&A*, 421, 1075
- Dullemond, C. P., & Spruit, H. C. 2005, *A&A*, 434, 415
- Dutrey, A., Semenov, D., Chapillon, E., et al. 2014, *ArXiv e-prints*, arXiv:1402.3503
- Favre, C., Cleeves, L. I., Bergin, E. A., Qi, C., & Blake, G. A. 2013, *ApJ*, 776, L38



- Fedele, D., Bruderer, S., van Dishoeck, E. F., et al. 2012, *A&A*, 544, L9
- Fogel, J. K. J., Bethell, T. J., Bergin, E. A., Calvet, N., & Semenov, D. 2011, *ApJ*, 726, 29
- Fraser, H. J., Collings, M. P., McCoustra, M. R. S., & Williams, D. A. 2001, *MNRAS*, 327, 1165
- Furuya, K., Aikawa, Y., Nomura, H., Hersant, F., & Wakelam, V. 2013, *ApJ*, 779, 11
- Garrod, R. T., Weaver, S. L. W., & Herbst, E. 2008, *ApJ*, 682, 283
- Glassgold, A. E., Galli, D., & Padovani, M. 2012, *ApJ*, 756, 157
- Glassgold, A. E., & Langer, W. D. 1973, *ApJ*, 179, L147
- Glassgold, A. E., Meijerink, R., & Najita, J. R. 2009, *ApJ*, 701, 142
- Glassgold, A. E., Najita, J., & Igea, J. 1997, *ApJ*, 480, 344
- . 2004, *ApJ*, 615, 972
- Gorti, U., & Hollenbach, D. 2009, *ApJ*, 690, 1539
- Hartmann, L., Calvet, N., Gullbring, E., & D'Alessio, P. 1998, *ApJ*, 495, 385
- Hasegawa, T. I., & Herbst, E. 1993, *MNRAS*, 261, 83
- Hasegawa, T. I., Herbst, E., & Leung, C. M. 1992, *ApJS*, 82, 167
- Heinzeller, D., Nomura, H., Walsh, C., & Millar, T. J. 2011, *ApJ*, 731, 115
- Henning, T., & Semenov, D. 2013, *Chemical Reviews*, 113, 9016
- Herczeg, G. J., Linsky, J. L., Valenti, J. A., Johns-Krull, C. M., & Wood, B. E. 2002, *ApJ*, 572, 310
- Herczeg, G. J., Wood, B. E., Linsky, J. L., Valenti, J. A., & Johns-Krull, C. M. 2004, *ApJ*, 607, 369
- Hindmarsh, A. C. 1983, in *Scientific Computing*, ed. R. S. Stepleman (Amsterdam: North-Holland), 55–64
- Hogerheijde, M. R., Bergin, E. A., Brinch, C., et al. 2011, *Science*, 334, 338
- Hollenbach, D., & McKee, C. F. 1979, *ApJS*, 41, 555
- . 1989, *ApJ*, 342, 306
- Kamp, I., Thi, W.-F., Meeus, G., et al. 2013, *A&A*, 559, A24
- Kippenhahn, R., Weigert, A., & Weiss, A. 2012, *Stellar Structure and Evolution*, Astronomy and Astrophysics Library (Springer)
- Krügel, E. 2008, *An Introduction to the Physics of Interstellar Dust*, Series in Astronomy and Astrophysics (Taylor & Francis Group)
- Laor, A., & Draine, B. T. 1993, *ApJ*, 402, 441
- Leger, A., Jura, M., & Omont, A. 1985, *A&A*, 144, 147
- Lynden-Bell, D., & Pringle, J. E. 1974, *MNRAS*, 168, 603
- Mathis, J. S., Ruml, W., & Nordsieck, K. H. 1977, *ApJ*, 217, 425
- Meijerink, R., Aresu, G., Kamp, I., et al. 2012, *A&A*, 547, A68
- Min, M., Dullemond, C. P., Dominik, C., de Koter, A., & Hovenier, J. W. 2009, *A&A*, 497, 155
- Mordaunt, D. H., Ashfold, M. N. R., & Dixon, R. N. 1994, *J. Chem. Phys.*, 100, 7360
- Nagy, B., Csontos, J., Kallay, M., & Tasi, G. 2010, *The Journal of Physical Chemistry A*, 114, 13213
- Najita, J. R., Carr, J. S., Pontoppidan, K. M., et al. 2013, *ApJ*, 766, 134
- Neufeld, D. A., & Kaufman, M. J. 1993, *ApJ*, 418, 263
- Neufeld, D. A., Lepp, S., & Melnick, G. J. 1995, *ApJS*, 100, 132
- Nomura, H. 2002, *ApJ*, 567, 587
- Öberg, K. I., Linnartz, H., Visser, R., & van Dishoeck, E. F. 2009a, *ApJ*, 693, 1209

- Öberg, K. I., van Dishoeck, E. F., & Linnartz, H. 2009b, *A&A*, 496, 281
- Owen, J. E., Ercolano, B., Clarke, C. J., & Alexander, R. D. 2010, *MNRAS*, 401, 1415
- Pontoppidan, K. M., Salyk, C., Bergin, E. A., et al. 2014, ArXiv e-prints, arXiv:1401.2423
- Pontoppidan, K. M., Salyk, C., Blake, G. A., & Käufl, H. U. 2010a, *ApJ*, 722, L173
- Pontoppidan, K. M., Salyk, C., Blake, G. A., et al. 2010b, *ApJ*, 720, 887
- Pontoppidan, K. M., Boogert, A. C. A., Fraser, H. J., et al. 2008, *ApJ*, 678, 1005
- Riviere-Marichalar, P., Ménard, F., Thi, W. F., et al. 2012, *A&A*, 538, L3
- Röllig, M., Ossenkopf, V., Jeyakumar, S., Stutzki, J., & Sternberg, A. 2006, *A&A*, 451, 917
- Ros, K., & Johansen, A. 2013, *A&A*, 552, A137
- Salyk, C., Pontoppidan, K. M., Blake, G. A., et al. 2008, *ApJ*, 676, L49
- Salyk, C., Pontoppidan, K. M., Blake, G. A., Najita, J. R., & Carr, J. S. 2011, *ApJ*, 731, 130
- Schindhelm, E., France, K., Herczeg, G. J., et al. 2012, *ApJ*, 756, L23
- Semenov, D., Henning, T., Helling, C., Ilgner, M., & Sedlmayr, E. 2003, *A&A*, 410, 611
- Sternberg, A., & Dalgarno, A. 1989, *ApJ*, 338, 197
- Stevenson, D. J., & Lunine, J. I. 1988, *Icarus*, 75, 146
- Tielens, A. 2005, *The Physics and Chemistry of the Interstellar Medium* (Cambridge University Press)
- Tielens, A. G. G. M., Tokunaga, A. T., Geballe, T. R., & Baas, F. 1991, *ApJ*, 381, 181
- Umebayashi, T., & Nakano, T. 1981, *PASJ*, 33, 617
- van Dishoeck, E. F., Bergin, E. A., Lis, D. C., & Lunine, J. I. 2014, ArXiv e-prints, arXiv:1401.8103
- van Dishoeck, E. F., Jonkheid, B., & van Hemert, M. C. 2006, *Faraday Discussions*, 133, 231
- Vandooren, J., Sarkisov, O. M., Balakhnin, V. P., & Van Tiggelen, P. J. 1991, *Chemical Physics Letters*, 184, 294
- Visser, R., van Dishoeck, E. F., & Black, J. H. 2009, *A&A*, 503, 323
- Woitke, P., Kamp, I., & Thi, W.-F. 2009a, *A&A*, 501, 383
- Woitke, P., Thi, W.-F., Kamp, I., & Hogerheijde, M. R. 2009b, *A&A*, 501, L5
- Woodall, J., Agúndez, M., Markwick-Kemper, A. J., & Millar, T. J. 2007, *A&A*, 466, 1197
- Zhang, K., Pontoppidan, K. M., Salyk, C., & Blake, G. A. 2013, *ApJ*, 766, 82